Imaging Lithosphere–Asthenosphere Interaction Beneath the North China Craton: Implications for Intraplate Volcanism and Anomalous Basin Subsidence

Bowen Li[a,b], Juan C. Afonso[b,c,d], Dinghui Yang[a,*], Mengxue Liu[e], Xingpeng Dong[e], Xiaobing Xu[a]

[a]*Department of Mathematical Sciences, Tsinghua University, Beijing, 100084, China*
[b]*Faculty of Geo-Information and Earth Observation (ITC), University of Twente, Enschede, the Netherlands*
[c]*School of Natural Sciences and CODES, University of Tasmania, Tasmania, 7001, Australia*
[d]*Department of Earth and Space Sciences, Southern University of Science and Technology, Shenzhen, Guangdong, China*
[e]*Institute of Geology, China Earthquake Administration, Beijing, 100029, China*

Abstract

The Datong volcanic field and the adjacent Bohai Bay Basin (BBB) in the North China Craton record contrasting Cenozoic histories. Datong shows sustained Quaternary intraplate volcanism, whereas the BBB exhibits anomalous post-rift subsidence since 12 Ma, greatly reduced Quaternary volcanism, and a recent decline in surface heat flow. These features are difficult to reconcile by prevailing tectonic models. Here we conduct probabilistic joint inversions of multiple and high-resolution geophysical datasets sensitive to the thermal structure of the lithosphere and sublithospheric mantle across the Datong–BBB region and surrounds. The results show a small-scale, three-dimensional circulation pattern with a deep mantle upwelling deflected by the Ordos lithospheric root toward Datong, paired with a coupled downwelling beneath the BBB. The deflected upwelling explains Datong volcanism, and the downwelling imposes negative dynamic topography that matches the magnitude and timing of the BBB's anomalous subsidence and is consistent with its declining heat flow and negligible Quaternary volcanism. These findings provide direct, observation-based constraints on asthenospheric flow and a single geodynamic explanation linking mantle dynamics to basin evolution in an intracontinental setting. To-

---

[*]Corresponding author
Email address: `ydh@mail.tsinghua.edu.cn` (Dinghui Yang)

gether, they resolve a major outstanding question in the Cenozoic evolution of the North China Craton.

Keywords: Geophysical joint inversion, North China Craton, Small-scale mantle convection, Datong volcanic field, Bohai Bay Basin anomalous subsidence

1. Introduction

Once a stable Archean craton, the North China Craton (NCC) underwent extensive modification and destruction during the Mesozoic and Cenozoic, particularly in its eastern part (ENCC) and Trans-North China Orogen (TNCO) (Zhu et al., 2012; Zhu and Xu, 2019; Griffin et al., 1998; Zhang et al., 2025a). Its Cenozoic evolution is widely attributed to subduction and rollback of the western Pacific plate, in conjunction with the far-field effect from the India-Eurasian continental collision, which established a regional extensional regime (cf. Zhu and Xu, 2019). This regime produced rift basins, including the Bohai Bay Basin (BBB) (Allen et al., 1997), and coincided with widespread intraplate volcanism. In the northeastern margin of the Ordos Block (OB), basaltic volcanism was extensive throughout the region, beginning in the Late Eocene-Oligocene and continuing through the Miocene into the Quaternary (Xu et al., 2004). Within this context, the Datong volcanic field represents the largest Quaternary volcanic center in the NCC (Xu et al., 2005). Seismic observations support this regional context. In particular, tomography studies identified a stagnant Pacific slab in the mantle transition zone (MTZ) beneath the ENCC (e.g., Huang and Zhao, 2006; Ma et al., 2019; Tao et al., 2018), and prominent low-velocity anomalies beneath Datong that extend into the MTZ. These low-velocity anomalies are commonly interpreted as hot and/or wet asthenospheric upwellings triggered by the deep dehydration of the stagnant Pacific slab (cf. Huang and Zhao, 2006; Xu et al., 2018, and references therein). This upwelling has also been suggested to deflect eastward, forming lateral mantle flow that modified the lithosphere, a process interpreted as being induced either by lithospheric delamination or rollback of the Pacific plate (Dong et al., 2021; Hao et al., 2025; Huang and Zhao, 2009; Guo et al., 2024).

While the rollback–upwelling framework can account for the intraplate volcanism in the region, it does not explain the post-rift evolution of the adjacent BBB. Three key observations are particularly difficult to reconcile with a simple upwelling/extension model: i) rapid Neogene–Quaternary subsidence that exceeds predictions from standard thermal-subsidence models (hereafter "anomalous subsidence") (e.g., Liu et al., 2022; Huang et al., 2014); ii) Quaternary volcanism within the basin is virtually absent despite vigorous intraplate activity in the adjacent Datong region; and iii) a decline of surface heat flow (SHF) in BBB during the latest 30 Ma (e.g., Qiu et al., 2015).

Several mechanisms have been advanced to explain the anomalous BBB signal, including a renewed rifting event (e.g., He and Wang, 2003), rapid thermal decay of previously upwelled asthenosphere (e.g., Guo et al., 2007) and fault reactivation (e.g., Huang et al., 2014). Each accounts for part of the record, but none reproduces (within a single, internally consistent framework) the combined constraints on subsidence amplitude and wavelength, volcanic distribution, and heat-flow evolution. Given these discrepancies, Liu et al. (2022) recently advocated a dynamic origin (small-scale convection) for the BBB's anomalous evolution over the past $\sim$12 Ma. This interpretation is consistent with seismic-based interpretations for the Songliao Basin to the north (Guo et al., 2016b; Liang et al., 2022). However, direct geophysical imaging of the subsurface thermal and density structure beneath the BBB is still lacking. Such information is essential to resolve the geometry and amplitude of mantle flow and to reconcile observations.

Here we jointly invert multiple geophysical observations to resolve the thermal and compositional structure of the lithosphere and sublithospheric mantle beneath the Datong-BBB region and surrounds. We employ a multi-observable probabilistic inversion framework (Afonso et al., 2013a,b, 2016) that integrates diverse geophysical datasets to enhance sensitivity to both thermal and chemical anomalies in the lithosphere. Using recent high-resolution observations, the in-

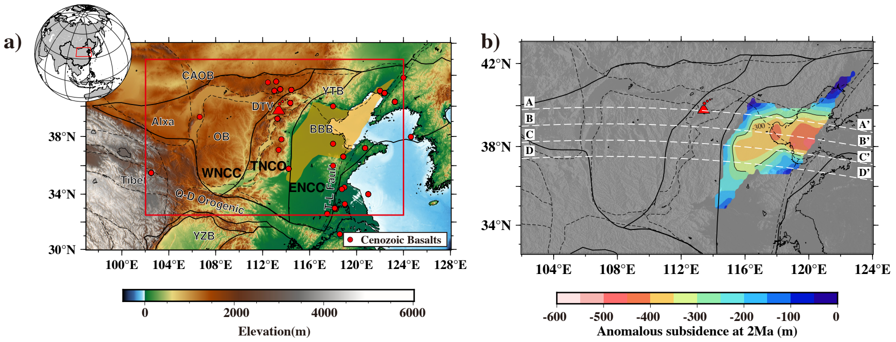

Figure 1: (a) Topography of the study region. Red rectangle shows our research area. Red circles show the spatial distribution of Cenozoic Basalts (taken from the Geochemistry of Rocks database). The orange overlay denote the Bohai Bay Basin (BBB). DTV, Datong volcanic field; CAOB, Central Asian Orogenic Belt; YTB, Yanshan Tectonic Belt; OB, Ordos Block; WNCC, Western North China Craton; TNCO, Trans North China Orogen; ENCC, Eastern North China Craton; Q-D, Qinling-Dabie; T-L, Tanlu; YZB, Yangtze Block. (b) Anomalous subsidence of BBB between ∼12 Ma and 2 Ma. The results refers to Liu et al. (2022)

version resolves an asthenospheric upwelling deflected by the Ordos lithospheric root and focused toward Datong, as well as a paired sublithospheric downwelling beneath the BBB. The diverted upwelling explains sustained intraplate volcanism at Datong, whereas the downwelling imposes negative dynamic topography leading to the BBB's anomalous post-rift subsidence and associated cooling. Together, these results reconcile previously conflicting observations and provide the missing, observation-based link between upper-mantle convection, intraplate volcanism, and the post-rift evolution of the BBB.

2. Geological Background

2.1. North China Craton (NCC)

The NCC can be divided into three primary units: the ENCC, the Western NCC (WNCC), and the TNCO between them (See Figure 1a) (Zhao et al., 2005). Once among one of the most stable Archean cratons, the NCC maintained a thick, refractory lithospheric mantle until the late Paleozoic (Zhu et al., 2012; Griffin et al., 1998). However, during the Mesozoic, the lithosphere beneath the ENCC underwent considerable modification. Its lithospheric thickness was reduced from $\sim$ 200 km to less than 80 km, and its originally depleted mantle was replaced by a more fertile composition. This transformation was accompanied by widespread magmatism and translithospheric faulting (Chen et al., 2009; Zheng et al., 2007; Griffin et al., 1998). In contrast, the WNCC has retained its stable cratonic characteristics, maintaining a thick and high seismic velocity lithosphere (Chen et al., 2009; Huang and Zhao, 2006). The major changes in the ENCC during the Mesozoic are widely attributed to the westward Paleo-Pacific plate subduction (Zhu and Xu, 2019). In the Early Cenozoic, the Paleo-Pacific slab is thought to have sunk into the deep mantle, while the Pacific plate continued to subduct and stagnate in the MTZ, and experienced rollback (Liu et al., 2019). This long-term dynamic process was accompanied by widespread eruption of basalts and extensional tectonics in the ENCC (Liu et al., 2019; Zhu and Xu, 2019; Zheng et al., 2007; Guo et al., 2016a; Zhang et al., 2025a).

2.2. Bohai Bay Basin (BBB)

The BBB is one of the largest Cenozoic rift basins in the ENCC and forms a major continental petroliferous basin (Allen et al., 1997). It is bounded by the Tan-lu (T-L) fault to the east, the TNCO to the west, and the Yanshan tectonic belt (YTB) to the north (Figure 1a). The tectonic evolution of the basin is generally divided into two stages: a Paleogene syn-rift stage and a Neogene–Quaternary post-rift stage (Allen et al., 1997). Previous studies have shown that the BBB has undergone anomalous subsidence since $\sim$12 Ma (Liu et al., 2022; Huang et al., 2014). Compared with classical stretching models (Jarvis and McKenzie, 1980), the BBB has experienced an average of $\sim$400 m anomalous subsidence to date (Liu et al., 2022). During the Quaternary, the rate of anomalous subsidence accelerated significantly. The spatial pattern of this rapid subsidence closely corresponds with active faulting within this period (Liu et al., 2022). Between $\sim$12 Ma and 2 Ma, more than 300 m of anomalous subsidence had already accumulated across the central BBB, with values reaching up to 450 m at the subsidence center. The spatial distribution shows a progressive decrease in subsidence magnitude toward the basin margins (Figure 1b).

The SHF in the BBB exhibits relatively high values, with an average value of 66 ± 11 $\mathrm{mW/m^2}$ (Liu et al., 2022). Thermal history studies of the BBB indicated that SHF increased during the Paleogene, and peaked in the middle-late Paleogene, reaching values above 80 $\mathrm{mW/m^2}$ (Qiu et al., 2015). Following the transition to the post-rift stage, SHF began a steady decline.

Geophysical studies suggest that the BBB has a relatively thin crust (31-34 km) and thin lithospheric mantle (60-80 km) (Zhang et al., 2019, 2025a). Thermo-rheological models indicate that long-term strength is retained only in the uppermost crust, whereas the middle-lower crust and underlying lithospheric mantle behave predominantly ductile (Liu et al., 2016). This configuration implies a weak lithosphere beneath BBB (Liu et al., 2016), which would make it susceptible to deformation by sublithospheric processes.

3. Data and Methods

3.1. Data

3.1.1. Seismic Data

The primary dataset of Rayleigh-wave dispersion curves for the period range of 10-120 sec was taken from the recent surface wave tomography model of Zhong et al. (2024). This dataset provides one of the densest and highest-resolution surface wave dispersion data to date for the entire NCC. It is based on teleseismic records from 1,355 portable stations (ChinaArray experiment) and 158 permanent seismic stations, with an average inter-station spacing of 35 km. For the peripheral regions not covered by the model of Zhong et al. (2024), we used dispersion curves from the study of Shen et al. (2016) together with those extracted from the full-waveform SinoScope1.0 velocity model (Ma et al., 2022). These two datasets were combined to construct complementary dispersion curves spanning periods of 10–140 s, and they exhibit excellent consistency in the overlapping period range (35–70 s). Depth sensitivity kernels of Rayleigh wave phase velocities (Supplementary Material Figure S10) show that longer-period dispersion retains appreciable sensitivity to depths near and below 200 km. Further details are provided in the Supplementary Material Text S1. It is important to note that the inclusion of these peripheral regions serves only to ensure geographic context and completeness; they are not incorporated into, nor do they affect, the interpretations or conclusions of this study.

As an additional, secondary constraint, we incorporated P-wave velocity information from the SinoScope1.0 tomographic model for the deepest parts of our model. Because these velocities are themselves the product of a regularized inversion rather than direct observations, we assigned relatively generous uncertainties to them (see Supplementary Material Figure S6). We also note that Vp is generally less sensitive to temperature than Vs. Therefore, by including this secondary constraint, we are only encouraging posterior models that honor the primary dispersion data well (our primary constrain on Vs), maintain thermodynamically-consistent relationships between Vs and Vp, and remain compatible with the Vp values inferred from SinoScope1.0.

3.1.2. Surface Heat Flow, Elevation and Geoid

SHF data were obtained from the newest China heat flow database (Wang et al., 2024) and the global database (Fuchs et al., 2023). To minimize the influence of shallow groundwater circulation, which are not representative of the deep lithospheric thermal structure, we excluded values below $20mW\,m^{-2}$ and above $120mW\,m^{-2}$. Elevation data were taken from the GTOPO30 global elevation model (http://lta.cr.usgs.gov/GTOPO30). We applied a low-pass filter to remove high-frequency content with wavelengths shorter than 50 km. Geoid height data were taken from the global model of Salajegheh and Afonso (2023). This filtered model considers only the effects of causative density anomalies at depths $>$ 400 km by removing deeper density anomalies (not modeled here) from the complete Earth Gravitational Model 2008 (Pavlis et al., 2012).

Uncertainties for elevation and geoid height were estimated in the following way. The study area was subdivided into 276 non-overlapping 1D columns forming a $1^\circ \times 1^\circ$ grid (this is twice the discretization used for dispersion data; see next section). For each column, we extracted all available data points in the respective datasets within the surface area of that column. From these values, we calculated both the mean and the variance. The mean values were taken as the representative input data for each column, whereas the variances were converted into standard deviations to provide the corresponding uncertainty estimates. Therefore, these uncertainties do not represent measurement errors, but rather the natural variability of the fields within the area of each column. Actual observational errors are considerably smaller and therefore not considered here.

3.2. Methods

We jointly invert the multiple datasets in Section 3.1 with the multi-observable probabilistic inversion method (Afonso et al., 2013a,b, 2016). This approach has been successfully applied to a wide range of datasets across different tectonic settings worldwide (e.g., Afonso et al., 2016, 2022; Qashqai et al., 2018; Guo et al., 2016a; Salajegheh et al., 2025; Shan et al., 2014). Full methodological details are provided in these references. Here, we summarize only the most relevant aspects to the present study. The study region is subdivided into 990 vertical columns with a surface area of $0.5^\circ \times 0.5^\circ$. While this discretization is sufficient to preserve the detail of the Rayleigh-wave dispersion curves, it is not compatible with the 1D assumption adopted in other forward problems (i.e., geoid, elevation, surface heat flow Afonso et al., 2013a,b, 2016). To reconcile these requirements, we aggregate four adjacent columns into larger $1^\circ \times 1^\circ$ units. Each aggregated unit is assigned a uniform value of elevation, geoid, and surface heat flow, as described in the previous section.

The inverse problem is casted as a statistical inference problem through Bayes' theorem (Tarantola, 2005). In this approach, the solution to the inverse problem is represented by a probability distribution over model parameters ($\boldsymbol{m}$) referred to as the posterior probability density function (PDF). The posterior is conditioned on the data and on the modeling assumptions (via the forward model, representation of errors and prior constraints) and represents the most general solution to the inverse problem (cf. Tarantola, 2005; Afonso et al., 2013a, see also Supplementary Material Text S2). To obtain estimates of the multidimensional posterior PDF, $\mathcal{P}(\boldsymbol{m})$, we use the Markov Chain Monte Carlo (MCMC) method based on the Delayed Rejection Adaptive Metropolis (DRAM) algorithm (Haario et al., 2006; Shan et al., 2014). Details on the algorithm can be found in the Supplementary Material and in Qashqai et al. (2018); Guo et al. (2016a); Shan et al. (2014)

The vertical parameterization of each column is illustrated in Supplementary Material Figure S5. Each 1D column includes a three- or four-layered crust, which consists of one sedimentary layer and two or three crystalline layers depending on the local crustal architecture. Each crustal layer is parameterized by seven variables: thermal conductivity (k), thermal expansivity (α), compressibility (β), bulk density (ρ), thickness (h), V_P/V_S ratio, and radiogenic heat production (RHP). The first three parameters are assumed known and constant (see Supplementary Material Table S2 and Salajegheh et al. (2025) for rationale), while the remaining four are treated as unknowns in the inversion. Initial estimates for sediment thickness are taken from the recent continental crust model for China (Xiao et al., 2021) and from CRUST1.0 in oceanic regions Laske et al. (2013). Initial Moho depths are taken from a previous receiver function study (Li et al., 2014). These initial values are updated within defined prior bounds (see Supplementary Material Table S3) during the inversion.

The upper mantle is subdivided into two compositional layers, namely the lithospheric and sublithospheric mantle (the model extends to a depth of 410 km). Each mantle layer is described by its thickness and its major-element composition within the CFMAS (CaO–FeO-MgO–Al_2O_3–SiO_2) system. While temperatures within the lithospheric mantle are determined at each simulation by solving the conductive heat transfer equation, those in the sublithospheric mantle are obtained by linear interpolation of temperatures at 3-5 inversion nodes (depending on the thickness of the lithospheric mantle). The temperatures at these nodes are treated as free model parameters, whose values are fully constrained by the data and estimated during the inversion (Salajegheh et al., 2025;

Afonso et al., 2016).

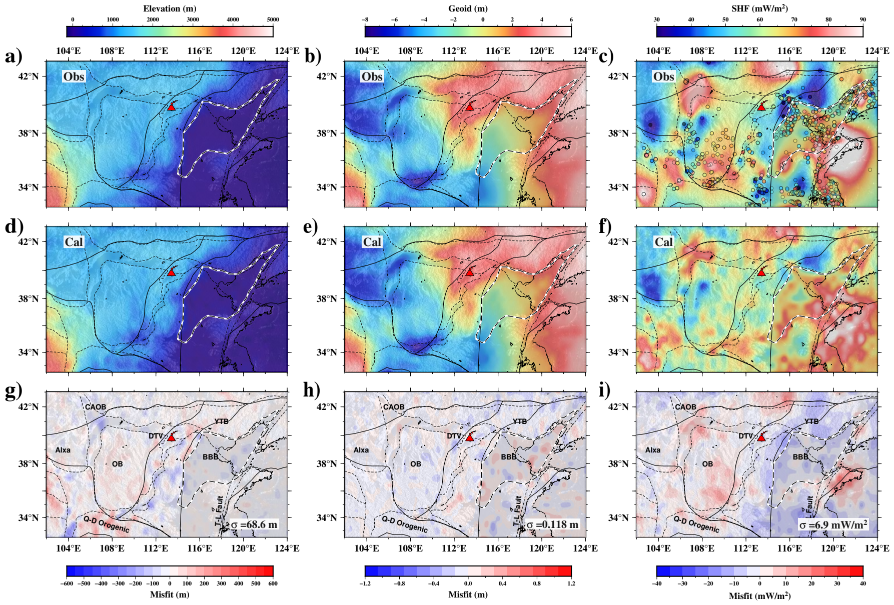

Figure 2: Observed (a-c) and predicted (d-f) elevation, geoid and SHF with their respective misfits (g-i); the standard deviations of the individual misfits are also included. The colored circles in panel (c) represent the raw SHF measurements. The red triangle denotes the Datong Volcanic Field, while the BBB region is outlined with bold solid lines.

4. Results

4.1. Data Fits

Figures 2, 3 and 4 provide a summary of the data-fit performance of our model. Unless indicated otherwise, predicted values correspond to their posterior mean estimates. Figure 2 compares observed and predicted values for all non-seismic datasets. Both predicted elevation and geoid anomalies agree closely with their observed counterparts, with low root-mean-square (RMS) misfits of 76.8 m and 0.116 m, respectively.

SHF displays the largest discrepancies (Figures 2 c-i), which is expected given the relatively high uncertainties associated with this observable. Nevertheless, the predicted SHF reproduces the first-order spatial pattern and amplitudes of the observations, and the misfits generally remain within the assumed uncertainty bounds across most of the study area.

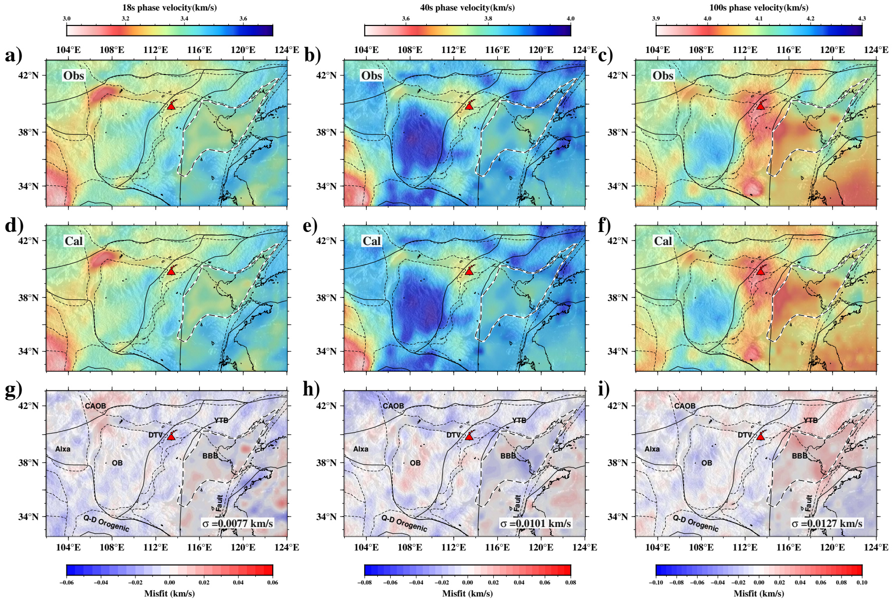

Figure 3: Observed (a-c) and predicted (d-f) Rayleigh phase velocity at 18, 40 and 100 sec. The misfits and their standard deviations are shown in panels (g-i). For reference, typical standard deviations of the observed phase velocities at 18, 40 and 100 s are 0.025, 0.035 and 0.06 km/s, respectively.

Figure 3 presents the observed and predicted Rayleigh wave phase velocities for three representative periods (18, 40, and 100 s). A similar comparison for P-wave velocities is shown in Figure 4. The predicted phase velocities are in excellent agreement with the observations at all periods, an important result since dispersion data constitute the main and highest resolution dataset available. The fit to P-wave velocities from the SinoScope1.0 model is less satisfactory. This outcome is expected, however, for two main reasons. First, Vp is treated as a secondary constraint only (Section 3.1.1), therefore they do not exert a strong control over the posterior models (Figure 4). Second, the inversion does not attempt a fit to Vp values from SinoScope1.0 at all depths, but instead targets discrete levels corresponding to the mantle thermodynamic nodes (Supplementary Material Figure S6). As a result, the predicted Vp reflects depth-averaged patterns rather than point-by-point values. Despite these limitations, our predicted Vp values are consistent with the first-order features

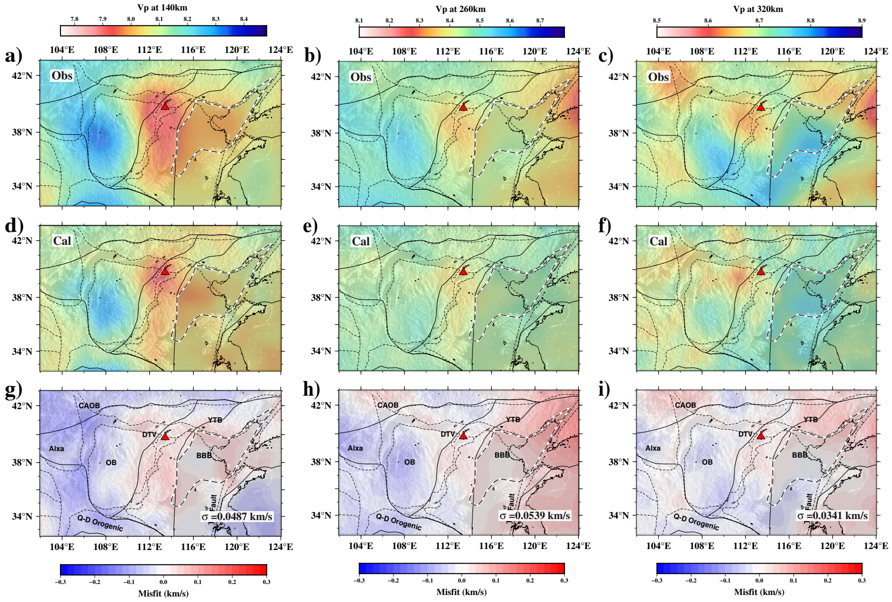

Figure 4: Observed (a-c) and predicted (d-f) P-wave velocity at 140, 260 and 320 km depth. The misfits and their standard deviations are shown in panels (g-i). We set 2% of the P-wave velocity value as uncertainty (see text for details). For reference, these uncertainties are approximately 0.162, 0.169, and 0.173 km/s at depths of 140, 260, and 320 km, respectively.

of the SinoScope1.0 velocity model, with misfits remaining within the prescribed uncertainty bounds at most depths.

4.2. Lithospheric thickness and compositional structure across the model

The lithosphere-asthenosphere boundary (LAB) is defined here as the 1,250°C isotherm (cf. Afonso et al., 2016; Guo et al., 2016a). Figure 5a presents a map of the posterior mean of LAB depth from our inversion. Two prominent regions of thick lithosphere (> 150 km) are found beneath known cratonic domains: one beneath the Ordos-Alxa blocks and another beneath the Yangtze Block (YZB). In contrast, the ENCC is characterized by a considerably thinner lithosphere, especially near the T-L Fault Zone and along the eastern coast, where lithospheric thickness is less than 60 km. This observation is consistent with other seismological studies (Zhang et al., 2019) and supports the interpretation of lithospheric modification in the ENCC (e.g., Zhu et al., 2012; Zhu and Xu, 2019; Guo et al., 2016a). Moreover, regions of thin lithosphere show an excellent spatial correlation with the distribution of Cenozoic basalts (Figure 5a). Shallow LAB values extend westward into the TNCO, tapering off toward the northern and eastern margins of the OB. The northeastern margin of the Tibetan Plateau, the northern segment of WNCC, and the YTB are also characterized by moderately thin lithosphere (90-110 km), thicker than in the ENCC but still considerably thinner than in the OB and YZB.

Following common practice, we use the bulk magnesium number, $\mathrm{Mg}^{\#} = 100 \times \mathrm{MgO}/(\mathrm{MgO} + \mathrm{FeO})$ to characterize lithospheric compositional heterogeneity. This proxy is an excellent indicator of mantle depletion or (re)fertility and correlates well with most physical parameters of interest (Afonso et al., 2010; Schutt and Lesher, 2006). Our results reveal that most of the NCC, including the ENCC, the southern TNCO and the western WNCC, is underlain by relatively normal (slightly depleted) lithospheric mantle, with average $\mathrm{Mg}^{\#}$ values of ~90 (Figure 5b). The most prominent departure from this pattern is the OB, which emerges as a consistently depleted block. This anomaly is particularly significant given that, owing to the limited sensitivity of the datasets to compositional variations and the assumptions inherent in our methodology (cf. Afonso et al., 2013a,b, 2016), the recovered amplitudes in regions with anomalous $\mathrm{Mg}^{\#}$ are likely underestimated.

To evaluate the predictive strength of our compositional model, we compare our predicted lithospheric $\mathrm{Mg}^{\#}$ PDFs against empirical distributions of peridotitic xenoliths from Cenozoic lavas at eight key localities in the NCC (Figure 6). A strong consistency between model predictions and observations is evident from the close correspondence of their mean values across most localities. The agreement is particularly good in sample-rich sites, such as Hannuoba, Yangyuan, and Nvshan (Figures 6a, b and g). This is a significant observation as the inversion does not include any local information from xenoliths; the compositional model is entirely retrieved by the inversion of geophysical data. The only significant mismatch between our predictions and xenolith data occurs in the Hebi region (Figure 6e), where the model suggests a less depleted litho-

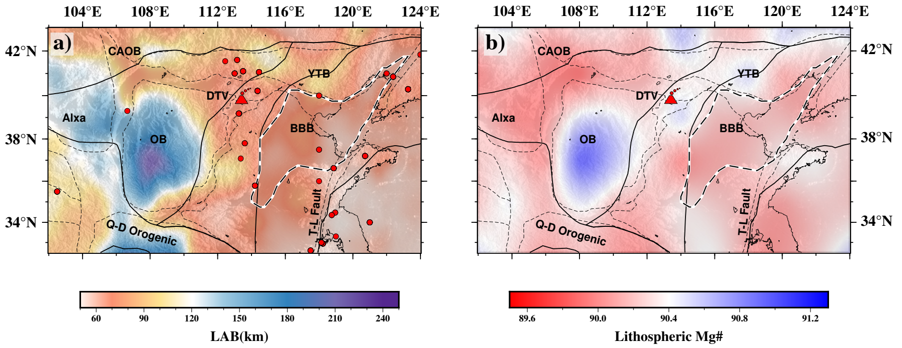

Figure 5: Predicted LAB depth (a) and depth-average lithospheric mantle Mg$^{\#}$ (b). Red circles in (a) represent the distribution of Cenozoic Basalts.

spheric mantle than indicated by the xenolith record. A similar discrepancy was reported by Guo et al. (2016a), who argued that shallow remnants of depleted lithosphere can persist locally beneath Archean blocks that have undergone extensive metasomatic or tectonic modification, and may subsequently be sampled by younger volcanism. This view was also advanced by Zheng et al. (2007) to explain the refractory character of the Hebi xenolith suite and by Bao et al. (2013) based on results from seismic tomography. The presence of a few fertile or refertilized samples within the limited dataset further supports this scenario. In addition, xenolith thermobarometry indicates a thin and anomalously hot lithosphere in this area (Zheng et al., 2007; Sun et al., 2012), consistent with our model predictions.

4.3. 3D Temperature Structure

The temperature structure within the lithosphere follows closely the variation pattern of the LAB (high/low thermal gradients correspond to shallow/deep LAB), as summarized in Figure S7 in the Supplementary Material. In the deeper mantle, our model reveals two prominent high-temperature anomalies, hereafter referred to as H1 and H2 (Figure 7). Anomaly H1 extends across much of the TNCO, with its eastern margin reaching the western boundary of the ENCC. Its spatial distribution closely matches regions characterized by thin lithosphere

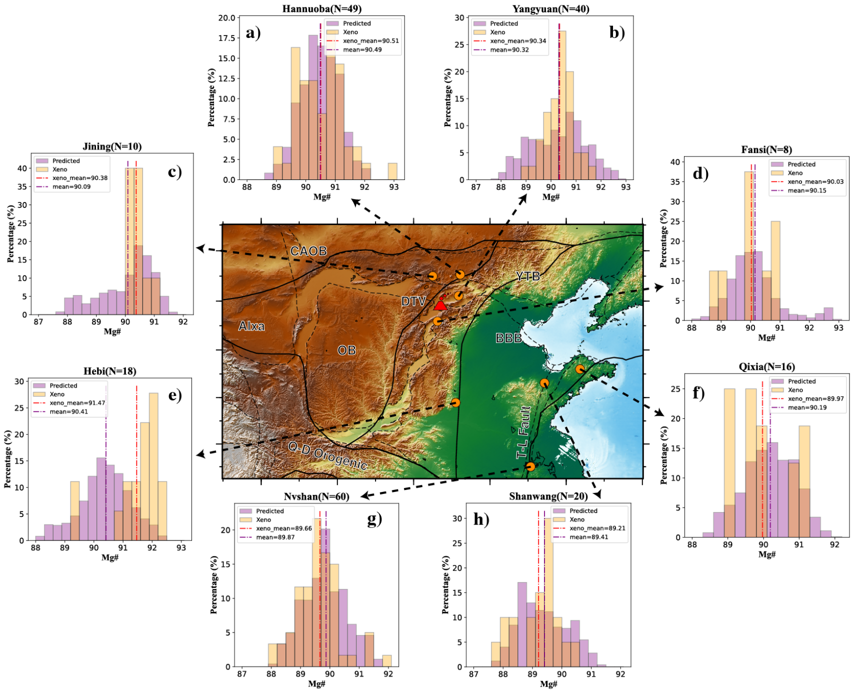

Figure 6: (a-h) Comparision of observed and predicted $Mg^{\#}$ of the lithospheric mantle in 8 localities across the NCC. purple histograms depict the final posterior PDFs given by our inversion; yellow histograms represent the observed distributions obtained from local xenolith samples (data from Xia et al. (2020); Zheng et al. (2007) references therein). Purple and red dashed line represent the means of observed and predicted data. Each panels give the number of xenolith samples used to obtain the observed distributions.

(Figure 5a). In addition, H1 is connected to a pseudo-vertical, plume-like thermal anomaly beneath the northeastern OB. Notably, the apex of H1 is not only located directly above this plume-like structure, but it also coincides with the Pleistocene-Holocene Datong volcanic field. This strongly suggests a genetic link between H1 and the intraplate volcanism in the region.

Anomaly H2 is mostly situated offshore, with its western boundary extending to the T-L fault. This anomaly aligns well with regions exhibiting lithospheric thinning (Figure 5a) and widespread Cenozoic basalts (Figure 1a). South of H2, the anomaly expands further and appears to merge/interact with anomaly H1 at the south of the ENCC. A somewhat pronounced low-temperature mantle anomaly beneath the northern ENCC separates the H1 and H2 anomalies.

Interestingly, the position of this anomaly coincides spatially with the region of the BBB that underwent significant subsidence between ∼12 and 2 Ma (white area in Figure 7; see also Section 2.2).

To further illustrate this spatial link, we extracted four vertical profiles of temperature and density anomalies across the BBB (Figures 8a-d and 8e-h, respectively). All profiles reveal coherent temperature and density structures that resemble convective-like patterns commonly observed in mantle convection simulations in the upper mantle. In particular, beneath the Datong volcanic field, the sub-lithospheric mantle displays a prominent high-temperature anomaly that is consistent with an upwelling that is diverted laterally by the thick lithospheric root of the OB. In contrast, the mantle beneath BBB consistently shows lower temperatures and high-density anomalies reminiscent of a small-scale sublithospheric downwelling. The northern tip of the H2 anomaly is also present on the eastern side of the transects. Although our results do not allow us to fully resolve its geometry, previous tomography studies suggest that this feature is linked to deeper upwellings originating from the stagnant Pacific slab (outside our study region) (Liang et al., 2022).

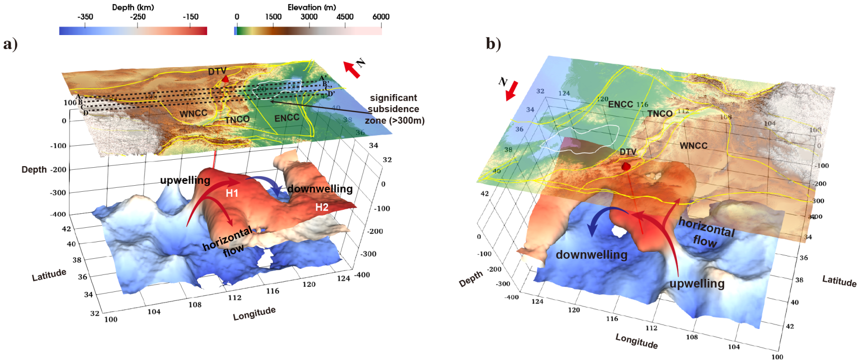

Figure 7: (a-b) 3D visualization of the subsurface temperature structure beneath the study region, showing the 1,400°C isosurface, colored by depth. The white-outlined region denotes the area of significant subsidence in the Bohai Bay Basin, where anomalous subsidence exceeds 300 m at 2 Ma (also shown in Figure 1b).

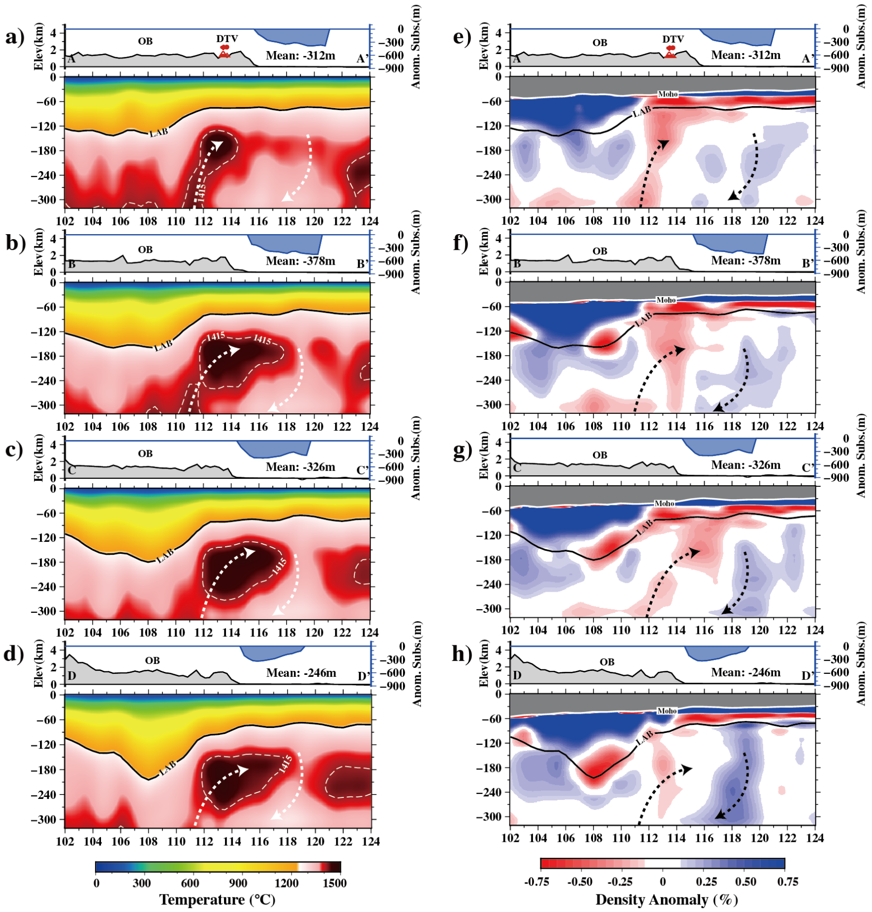

Figure 8: Vertical temperature (a-d) and density anomaly (e-h) cross-sections along the profiles in Figure 7a and Figure 1b. Grey shading (left axis) shows elevation along the profile; blue shading (right axis) indicates anomalous subsidence at ∼2 Ma (prior to Quaternary fault deformation) with mean value given.

5. Discussion

5.1. The Effect of Different Input P-wave Models on Inversion Results

As mentioned in Section 3, our inversion incorporated P-wave velocities from the SinoScope1.0 tomographic model (Ma et al., 2022) as a secondary constraining dataset. Because the uncertainty of surface-wave dispersion data generally increases with depth, it is important to evaluate how sensitive our results are to the assumed Vp structure. We therefore repeated the joint inversion using two additional, independent Vp models: Tao18 (Tao et al., 2018), derived from full-waveform inversion, and Guo24 (Guo et al., 2024), based on travel-time tomography (see Supplementary Material Figure S11–S14).

Above ∼200 km, the inferred thermal structures are nearly identical across all tested models, reflecting the strong resolving power of surface-wave dispersion at these depths and the consistency between the different Vp models. Below ∼200 km, the recovered thermal patterns tend to follow the lateral variations in Vp models more closely, although overall consistency among the resulting thermal models remains high. The largest differences are associated with the Guo24 model. Since this model is based on relative travel-time tomography, we consider the SinoScope and Tao18 results to be more reliable in terms of absolute velocities. Importantly, the first-order features of high temperature beneath the Datong volcanic field and low temperature beneath the BBB remain consistent across all tested Vp models.

5.2. Comparison With Previous Studies

In recent years, numerous studies have investigated lithospheric thickness beneath the NCC using different approaches, including thermal modeling (e.g., Zhang et al., 2025a; Sun et al., 2022), seismic tomography (e.g., Li et al., 2022), and receiver functions (e.g., Zhang et al., 2019). Despite differences in methodology and physical definitions, these models consistently reveal similar first-order features: a relatively thin lithosphere beneath the ENCC and a thicker lithosphere beneath the WNCC, particularly the OB region (see Supplementary Material Figure S15).

Differences mainly appear in second-order structures (see Supplementary Material Figure S15). For example, the receiver function–derived LAB Zhang et al. (2019) displays local discrepancies in regions such as the southern TNCO and northeastern OB. These discrepancies likely reflect the different sensitivities of the various methods to the LAB. Receiver function studies are most sensitive to seismic impedance contrasts, which in some cases can coincide with the base of the lithosphere but may also reflect other sharp compositional or rheological transitions. In contrast, thermal models and surface-wave tomography typically delineate the LAB using a thermal criterion (e.g., a reference isotherm) or velocity criterion, such as the depth at which velocity gradients change. Furthermore, even among thermally defined LAB models, differences may arise due to different seismic datasets used and/or the inversion strategies employed. Thermal models constrained solely by seismic velocities (e.g., Sun et al., 2022) may also differ from those incorporating multi-observational constraints (e.g., Zhang et al., 2025a). Notably, our LAB geometry and depth variations are highly consistent with the recent thermal model of Zhang et al. (2025a).

Figures S8 and S9 in the Supplementary Material compare our results with the recent thermochemical model of Zhang et al. (2025a) (hereafter Z2025), a study that used a similar inversion technique to ours, but with different datasets. From the surface down to 200 km depth, both models reproduce nearly identical first-order structures, including LAB geometry and lithospheric $\mathrm{Mg}^{\#}$. This agreement, together with the general consistency with full-waveform tomography models discussed in the previous section, lends credibility to our first-order thermal structure for the region. Nevertheless, several regional differences are evident. Z2025 infers a somewhat thinner lithosphere beneath the Alxa block compared to our results. The discrepancy in LAB depth likely reflects differences in the dispersion datasets employed in the two studies (e.g., Afonso et al., 2016; Zhang et al., 2025a). Our dispersion dataset provides a denser spatial coverage, particularly around the Alxa block, compared to that used by Z2025, which may partly account for the thicker lithosphere inferred in our model. Independent tomographic studies also image high-velocity features at ∼200 km depth beneath Alxa (e.g., Guo et al., 2024; Tao et al., 2018), consistent with a relatively thick LAB in this region.

For lithospheric Mg$^{\#}$, discrepancies likely reflect a combination of differences in seismic data constraints and model/crust parameterizations (Afonso et al., 2016; Zhang et al., 2025a; Afonso et al., 2022). Since Mg$^{\#}$ is indirectly constrained through its influence on density and seismic velocities, variations in the dispersion datasets and in priors on crustal structure can propagate into compositional differences in the recovered models. Despite this, both inversions yield remarkably similar Mg$^{\#}$ spatial patterns across the regions central to this study, especially considering that absolute amplitudes of Mg$^{\#}$ anomalies are considerably uncertain in both studies due to methodological limitations (cf. Afonso et al., 2013a, 2016; Zhang et al., 2025a). The main exception is towards the southwestern domains, where the seismic datasets used on both studies show greater differences.

Below 200 km depth, the two models further diverge. Specifically, Z2025 favors slightly higher average temperatures and smoother, longer-wavelength patterns, whereas our model preserves finer-scale heterogeneity. This discrepancy largely reflects differences in seismic data, as we use a higher-resolution dispersion dataset and additional Vp information towards the bottom of our model (Section 3.1.1). At these depths, the spatial distribution of thermal anomalies broadly corresponds to lateral variations in Vp (see Supplementary Figures S11–S12). In this context, we note that a similar sublithospheric variability was also recognized in the thermal model of Guo et al. (2016a) and is consistent with independent seismic tomographic studies (e.g., Liang et al., 2022; Xu et al., 2018).

5.3. Explaining Post-Rift Subsidence of the BBB

Previous studies have revealed that the BBB experienced accelerated subsidence during its post-rift phase that cannot be explained by a standard basin evolution model (Allen et al., 1997; Liu et al., 2022; Huang et al., 2014; Guo et al., 2007). Several hypotheses have been proposed to account for this, including 1) a renewed phase of rifting (He and Wang, 2003), 2) fast and extensive cooling of the upwelled asthenosphere (Guo et al., 2007), 3) reactivation of faults (Huang et al., 2014) and 4) dynamic topography driven by mantle convection (Liu et al., 2022). In Liu et al. (2022), the authors excluded hypotheses 1) and 2), as they contradict thermal history studies reporting continuous decrease in SHF during the Neogene and Quaternary (Qiu et al., 2015). Furthermore, proposal 3) is thought to have influenced subsidence mainly during the Quaternary. Collectively, these observations made Liu et al. (2022) favor dynamic effects to explain the anomalous subsidence of BBB. However, no direct evidence was presented for an asthenospheric convection pattern capable of driving the observed subsidence of the BBB.

The temperature and density structures recovered by our inversion (Figures 7 and 8) provide evidence for an ongoing sublithospheric mantle convection pattern linking the Datong volcanic field with the BBB. Interestingly, the downwelling limb of this convection cell correlates with the location of anomalous subsidence observed in the BBB, lending further confidence to the convection scenario.

A number of tomography studies have also identified a high-velocity anomaly in the asthenosphere beneath the BBB, which spatially aligns with the low-temperature anomaly imaged in our model (e.g., Hao et al., 2025; Huang and Zhao, 2009; Xu et al., 2018). However, this anomaly has generally been interpreted as lithospheric fragments resulting from delamination events during the Cenozoic (Hao et al., 2025; Huang and Zhao, 2009). Two exceptions are the studies of Guo et al. (2016a) and Liang et al. (2022). The former reported similar low-temperature and high-density features beneath the ENCC (and BBB) and interpreted them as return or forced downwellings. The latter combined radial-anisotropy observations with tomography and concluded that the anomaly beneath the BBB region was consistent with a sublithospheric mantle downwelling. In this context, we also note that delamination episodes are expected to be accompanied by rapid surface uplift (Göğüş and Pysklywec, 2008), elevated SHF

(Schott and Schmeling, 1998) and magmatic activity. However, none of these phenomena have been observed in the BBB.

Taken together, the observations outlined above and our temperature–density results provide consistent evidence for a sublithospheric downwelling beneath the BBB and offer a coherent, physically plausible explanation for its anomalous subsidence.

To assess the potential dynamic subsidence that the imaged downwelling would produce, we carried out a quantitative analysis following the approach of Marquart and Schmeling (1989). Their numerical framework allows evaluating the influence of parameters such as lithospheric effective elastic thickness (T_e), the aspect ratio of convection cells, and the Rayleigh number steady-state on the resultant dynamic topography. In our calculations, we adopt a standard Rayleigh number of 10^5 (e.g., Marquart and Schmeling, 1989) and a convection cell aspect ratio of 1.33–1.78, corresponding to a vertical height of 450 km (i.e. upper mantle small-scale convection) and a width of 600–800 km (Figure 8). The T_e was estimated from the lithospheric rheological profile, calculated from our inverted density and temperature structures (See Supplementary Materials Text S3 and Figure S3). The resultant T_e values range between 15 and 25 km. Considering the latter value as a conservative estimate, our scaling analysis indicates that the imaged convection cell would produce steady-state dynamic subsidence of approximately 740 ± 90 m at the center of the downwelling (See Supplementary Materials Figure S4). At $\sim$2 Ma, the anomalous subsidence observed in the BBB has been estimated to be around 350–450 m (Figure 1b), an amount that is readily accounted for by the small-scale downwelling resolved imaged in our model. The difference between the observed and calculated amplitudes is expected, as i) the BBB cell is unlikely to be in perfect steady state, and ii) the analytic estimate assumes two-dimensional rolls, which yields an upper bound on dynamic topography (finite-length, three-dimensional cells produce lower amplitudes) (e.g., Zhang et al., 2025b).

5.4. Upper Mantle Dynamics Beneath the NCC

It is widely accepted that Pacific plate subduction plays a key role in the Cenozoic tectonic evolution of the NCC (Allen et al., 1997). Tomographic images consistently reveal a continuous high-velocity anomaly in the MTZ beneath the ENCC and TNCO (Ma et al., 2019; Liang et al., 2022), generally interpreted as the stagnant Pacific slab. Receiver function studies further indicate a thickened MTZ in this region, with its edge reaching as far as the Datong volcanic field (Sun et al., 2020). The stagnant slab is thought to release fluids through dehydration reactions (e.g., Huang and Zhao, 2006; Xu et al., 2018), promoting mantle upwelling above and around its leading edge; these hot/wet upwellings would explain the low-velocity anomalies imaged beneath the ENCC and TNCO (Huang and Zhao, 2006; Dong et al., 2021; Ma et al., 2019).

Geochemical studies have shown that the Fansi and Hannuoba basalts (locations shown in Figures 6 a and d) are similar in both composition and age (∼25 Ma) (Tang et al., 2006). Based on the isotopic characteristics, they suggest that the basaltic magmatism was likely induced by asthenospheric upwelling beneath the Datong region. Interestingly, the onset of volcanism around the Datong area predates, and then becomes broadly coeval with, the transition of the BBB into an anomalous post-rift subsidence phase. We infer that the asthenospheric upwelling imaged beneath the Datong region is dynamically linked to a paired sublithospheric downwelling beneath the BBB, consistent with our present-day temperature–density structure. This interpretation is further supported by regional shear-wave splitting (e.g., Zhu and Ma, 2021; Qiang et al., 2021; Liu et al., 2021) and radial anisotropy observations (e.g., Liang et al., 2022). The shear-wave splitting results show predominantly NW–SE–oriented fast polarization directions between the Datong volcanic field and the BBB, indicative of lateral mantle flow beneath the TNCO, whereas at depths greater than 100 km, radial anisotropy reveals a transition toward a more vertical anisotropic fabric beneath the BBB (see Supplementary Material Figure S16). In this view, recurrent upwelling focuses melt and volcanism at Datong, whereas the coeval downwelling beneath the BBB generates negative dynamic topography and cooling, accounting for both the amplitude and timing of the basin's anomalous subsidence and its negligible Quaternary volcanism. Recent 3D geodynamic simulations (Manjón-Cabeza Córdoba and Ballmer, 2022; Duvernay et al., 2022) are consistent with this scenario, showing that upwellings interacting with a cratonic keel (e.g., Ordos block) are easily deflected toward regions of thinner lithosphere. When they reach these regions, they promote downwellings (forced return flow). The younger volcanism in the Datong volcanic field, generally dated to 0.4–0.79 Ma (Xu et al., 2005), may record the persistence (and possible intensification) of this mantle upwelling, with early Cenozoic magmatism marking its onset.

A more comprehensive view of the regional mantle dynamics can be achieved by incorporating the high-temperature anomalies H1 and H2 shown in Figure 7. In our interpretation of the Datong-BBB mantle convection scenario, the northern segment of H1 is the uppermost expression of a deeper asthenospheric upwelling that is deflected around the lithospheric root of the OB. The Datong volcanic field lies on the thinner-lithosphere side of a pronounced lithospheric-thickness step (Figure 5a), where asthenospheric flow is naturally focused. This configuration provides an ideal locus for partial melting of the upwelling asthenosphere and the associated volcanism in the Datong region.

The circulation beneath the region is strongly three-dimensional, and the H1 anomaly likely includes a substantial lateral (quasi-horizontal) flow component along much of the TNCO. This interpretation is supported by widespread low-velocity anomalies reported in regional tomography (e.g., Xu et al., 2018; Liang et al., 2022; Bao et al., 2013, 2015), together with positive radial anisotropy in the asthenosphere and a nearly north–south oriented azimuthal anisotropy, both consistent with dominantly horizontal mantle fabric and organized lateral flow (Liang et al., 2022). We therefore infer that part of the upwelling is deflected southward (Figure 9), which may have contributed to LAB thinning and surface uplift in the TNCO (Li et al., 2024; Zhang et al., 2025a). In addition, the convergence of H1 with H2 in our model, together with widespread low-velocity anomalies in the southeastern NCC (Liang et al., 2022; Ouyang et al., 2014), implies that hot material from the southeast may also feed into the southern H1. As noted earlier, the northern segment of H2 is often interpreted as upwelling originating from the subducting Pacific slab (Liang et al., 2022), potentially contributing to generating the forced downwelling beneath the BBB.

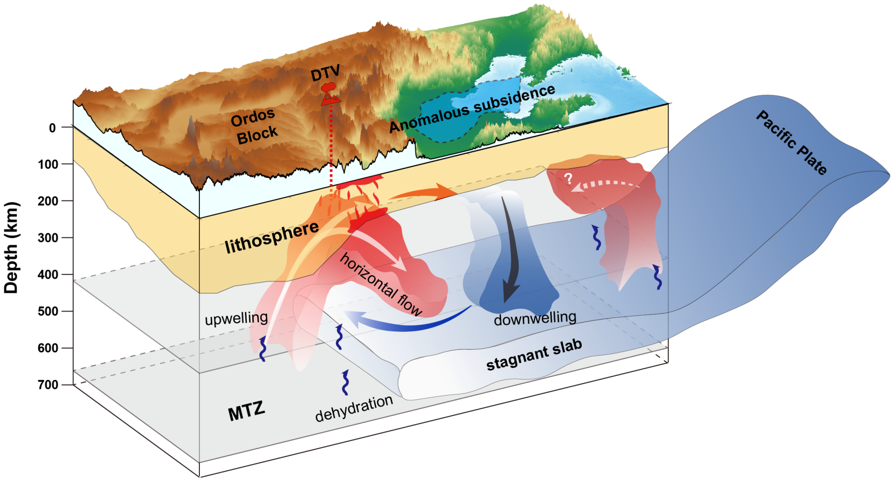

Figure 9: Schematic model of small-scale mantle convection beneath the NCC. The upwelling is likely initiated by fluids released from a stagnant slab through dehydration reactions (Huang and Zhao, 2006; Xu et al., 2018). These upwelling materials are diverted laterally by the thick lithospheric root of the Ordos Block, resulting in flow convergence toward the DTV, partial melting and volcanism. As the upwelling interacts with the thick lithosphere, it is deflected toward regions of thinner lithosphere. Upon reaching the BBB area, it promotes a downwelling via a forced return flow. A portion of the upwelling is also diverted southward, forming a sub-horizontal mantle flow. To the east, a secondary upwelling (e.g., Liang et al., 2022) may also contribute to the development of the forced downwelling beneath the BBB.

6. Conclusions

By jointly inverting multiple geophysical datasets, we have developed a thermochemical model of the lithosphere and sublithospheric mantle beneath the North China Craton, providing new insights into the coupling between mantle dynamics and surface processes. The results reveal a small-scale convection system composed of an upwelling beneath the Datong volcanic field and a compensating downwelling beneath the Bohai Bay Basin. This dynamic link offers a unified explanation for two first-order observations: sustained Cenozoic intraplate volcanism in the Datong region and the anomalous post-rift subsidence of the Bohai Bay Basin.

Taken together with previous seismic tomography studies, our results indicate that the Datong upwelling originates at depths pertaining to the mantle transition zone, potentially triggered by dehydration of the stagnant Pacific slab (Huang and Zhao, 2006; Xu et al., 2018). It is subsequently deflected by the Ordos lithospheric root, causing flow convergence towards the Datong region, where reduced lithospheric thickness promotes ascent and melt generation. We showed that the paired downwelling beneath the Bohai Bay Basin accounts for the anomalous subsidence since $\sim$ 12 Ma, tying basin evolution to ongoing sub-lithospheric circulation. These findings reconcile previously incompatible observations and highlight the critical and ongoing role of lithosphere-asthenosphere interactions in shaping the geodynamic and tectonic history of the North China Craton.

Declaration of competing interest

The authors declare that they have no known competing financial interests or personal relationships that could have appeared to influence the work reported in this paper.

Acknowledgments

We thank the editor Carolina Lithgow-Bertelloni and two reviewers for their constructive suggestions. B. Li and D. Yang acknowledge support from the Deep Earth Probe and Mineral Resources Exploration-National Science and Technology Major Project (Grant No. 2025ZD1004901). J.C. Afonso acknowledges support from the European Union's [Horizon 2020/Horizon Europe] research and innovation program under the MSCA (No. 101120556) and the European Space Agency under the 4D Earth program (4000140327/23/NL/SD). We gratefully acknowledge Prof. J. Wu for generously sharing the high-resolution Rayleigh-wave dispersion data used in this study. We also sincerely thank X. Liang for providing the radial anisotropy (RAN) results, B. Xia for compiling and sharing the xenolith geochemical dataset, and Q. Liu for supplying detailed data on the anomalous subsidence of the Bohai Bay Basin.

References

Afonso, J., Ben-Mansour, W., O'Reilly, S., Griffin, W., Salajegheh, F., Foley, S., Begg, G., Selway, K., Macdonald, A., Januszczak, N., Fomin, I., Nyblade, A., Yang, Y., 2022. Thermochemical structure and evolution of cratonic lithosphere in central and southern africa. Nature Geoscience 15, 405–410.

Afonso, J., Fullea, J., Griffin, W., Yang, Y., Jones, A., Connolly, J., O'Reilly, S., 2013a. 3-d multiobservable probabilistic inversion for the compositional and thermal structure of the lithosphere and upper mantle. i: a priori petrological information and geophysical observables. Journal of Geophysical Research: Solid Earth 118, 2586–2617.

Afonso, J., Fullea, J., Yang, Y., Connolly, J., Jones, A., 2013b. 3-d multi-observable probabilistic inversion for the compositional and thermal structure of the lithosphere and upper mantle. ii: General methodology and resolution analysis. Journal of Geophysical Research: Solid Earth 118, 1650–1676.

Afonso, J., Ranalli, G., Fernàndez, M., Griffin, W., O'Reilly, S., Faul, U., 2010. On the vp/vs–mg# correlation in mantle peridotites: Implications for the identification of thermal and compositional anomalies in the upper mantle. Earth and Planetary Science Letters 289, 606–618.

Afonso, J., Rawlinson, N., Yang, Y., Schutt, D., Jones, A., Fullea, J., Griffin, W., 2016. 3-d multiobservable probabilistic inversion for the compositional and thermal structure of the lithosphere and upper mantle:iii. thermochemical tomography in the western-central u.s. Journal of Geophysical Research: Solid Earth 121, 7337–7370.

Allen, M., Macdonald, D., Zhao, X., Vincent, S., Brouet-Menzies, C., 1997. Early cenozoic two-phase extension and late cenozoic thermal subsidence and inversion of the bohai basin, northern china. Marine and Petroleum geology 14, 951–972.

Bao, X., Song, X., Li, J., 2015. High-resolution lithospheric structure beneath mainland china from ambient noise and earthquake surface-wave tomography. Earth and Planetary Science Letters 417, 132–141.

Bao, X., Song, X., Xu, M., Wang, L., Sun, X., Mi, N., Yu, D., Li, H., 2013. Crust and upper mantle structure of the north china craton and the ne tibetan plateau and its tectonic implications. Earth and Planetary Science Letters 369, 129–137.

Chen, L., Cheng, C., Wei, Z., 2009. Seismic evidence for significant lateral variations in lithospheric thickness beneath the central and western north china craton. Earth and Planetary Science Letters 286, 171–183.

Dong, X., Yang, D., Niu, F., Liu, S., Tong, P., 2021. Adjoint traveltime tomography unravels a scenario of horizontal mantle flow beneath the north china craton. Scientific reports 11, 12523.

Duvernay, T., Davies, D., Mathews, C., Gibson, A., Kramer, S., 2022. Continental magmatism: The surface manifestation of dynamic interactions between cratonic lithosphere, mantle plumes and edge-driven convection. Geochemistry, Geophysics, Geosystems 23, e2022GC010363.

Fuchs, S., Neumann, F., Norden, B., Beardsmore, G., Chiozzi, P., Colgan, W., Anguiano Dominguez, A.P., Duque, M.R.A., Ojeda Espinoza, O.M., Forster, F., Förster, A., Fröhder, R., Fuentes, K., Hajto, M., Harris, R., Jõeleht, A., Liebing, H., Liu, S., Lüdtke, G., Madon, M., Negrete-Aranda, R., Poort, J., Reznik, I.J., Riedel, M., Rolandone, F., Stål, T., Verdoya, M., Wu, J.N., 2023. The global heat flow database: Update 2023. URL: `https://doi.org/10.5880/fidgeo.2023.008`.

Göğüş, O., Pysklywec, R.N., 2008. Near-surface diagnostics of dripping or delaminating lithosphere. Journal of Geophysical Research: Solid Earth 113.

Griffin, W., Andi, Z., O'Reilly, S., Ryan, C., Flower, M., Chung, S., Lo, C., Lee, T., 1998. Mantle dynamics and plate interactions in east asia. Geodynamics Series. American Geophysical Union, Washington, DC , 107–126.

Guo, H., Zhao, D., Ding, Z., 2024. Anisotropic tomography and mantle dynamics of the north china craton. Geophysical Journal International 236, 1455–1470.

Guo, X., Shi, X., Qiu, X., Wu, Z., Yang, X., 2007. Cenozoic post-rift unconformity and the accelerated subsidence events of the jiyang depression, bohai bay basin and preliminary analyses on their original mechanism. Chinese Journal of Geophysics 50, 412–422.

Guo, Z., Afonso, J., Qashqai, M., Yang, Y., Chen, Y., 2016a. Thermochemical structure of the north china craton from multi-observable probabilistic inversion: Extent and causes of cratonic lithosphere modification. Gondwana Research 37, 252–265.

Guo, Z., Chen, Y., Ning, J., Yang, Y., Afonso, J., Tang, Y., 2016b. Seismic evidence of on-going sublithosphere upper mantle convection for intra-plate volcanism in northeast china. Earth and Planetary Science Letters 433, 31–43.

Haario, H., Laine, M., Mira, A., Saksman, E., 2006. Dram: efficient adaptive mcmc. Statistics and computing 16, 339–354.

Hao, A., Zhang, H., Liu, L., Dai, L., Han, S., Fang, W., Wan, B., 2025. Cenozoic destruction of eastern north china craton evidenced by seismically imaged lithosphere delamination and nd isotopes. The Innovation Geoscience , 100144–1.

He, L., Wang, J., 2003. Cenozoic thermal history of the bohai bay basin: Constraints from heat flow and coupled basin–mountain modeling. Physics and Chemistry of the Earth, Parts A/B/C 28, 421–429.

Huang, J., Zhao, D., 2006. High-resolution mantle tomography of china and surrounding regions. Journal of Geophysical Research: Solid Earth 111.

Huang, J., Zhao, D., 2009. Seismic imaging of the crust and upper mantle under beijing and surrounding regions. Physics of the Earth and Planetary Interiors 173, 330–348.

Huang, L., Liu, C., Wang, Y., Zhao, J., Mountney, N., 2014. Neogene–quaternary postrift tectonic reactivation of the bohai bay basin, eastern china. AAPG bulletin 98, 1377–1400.

Jarvis, G., McKenzie, D., 1980. Sedimentary basin formation with finite extension rates. Earth and Planetary science letters 48, 42–52.

Laske, G., Masters, G., Ma, Z., Pasyanos, M., 2013. Update on crust1.0 - a 1-degree global model of earth's crust, in: Geophysical research abstracts, p. 2658.

Li, M., Song, X., Li, J., Bao, X., 2022. Crust and upper mantle structure of east asia from ambient noise and earthquake surface wave tomography. Earthquake Science 35, 71–92.

Li, Y., Gao, M., Wu, Q., 2014. Crustal thickness map of the chinese mainland from teleseismic receiver functions. Tectonophysics 611, 51–60.

Li, Z., Hao, M., Hammond, W.C., Cheng, F., Zhang, G., Wang, Q., Liu, L., Hou, B., Gan, W., 2024. Geodetic constraints on three-component motion of the ordos block (china) and their implications for lithospheric dynamics. Geological Society of America Bulletin 136, 5217–5230.

Liang, X., Zhao, D., Xu, Y., Hua, Y., 2022. Anisotropic tomography and dynamics of the big mantle wedge. Geophysical Research Letters 49, e2021GL097550.

Liu, J., Cai, R., Pearson, D., Scott, J., 2019. Thinning and destruction of the lithospheric mantle root beneath the north china craton: A review. Earth-Science Reviews 196, 102873.

Liu, J., Wu, J., Wang, W., Cai, Y., Fang, L., 2021. Seismic anisotropy and implications for lithospheric deformation beneath the ordos block and surrounding regions. Geophysical Journal International 226, 1885–1896.

Liu, Q., He, L., Yi, Z., Zhang, L., 2022. Anomalous post-rift subsidence in the bohai bay basin, eastern china: Contributions from mantle process and fault activity. Tectonics 41, e2021TC006748.

Liu, Q., Zhang, L., Zhang, C., He, L., 2016. Lithospheric thermal structure of the north china craton and its geodynamic implications. Journal of Geodynamics 102, 139–150.

Ma, J., Bunge, H., Thrastarson, S., Fichtner, A., Herwaarden, D.V., Tian, Y., Chang, S., Liu, T., 2022. Seismic full-waveform inversion of the crust-mantle structure beneath china and adjacent regions. Journal of Geophysical Research: Solid Earth 127.

Ma, J., Tian, Y., Zhao, D., Liu, C., Liu, T., 2019. Mantle dynamics of western pacific and east asia: New insights from p wave anisotropic tomography. Geochemistry, Geophysics, Geosystems 20, 3628–3658.

Manjón-Cabeza Córdoba, A., Ballmer, M.D., 2022. The role of edge-driven convection in the generation ofvolcanism–part 2: Interaction with mantle plumes, applied to the canary islands. Solid Earth 13, 1585–1605.

Marquart, G., Schmeling, H., 1989. Topography and geoid undulations caused by small-scale convection beneath continental lithosphere of variable elastic thickness. Geophysical Journal International 97, 511–527.

Ouyang, L., Li, H., Lü, Q., Yang, Y., Li, X., Jiang, G., Zhang, G., Shi, D., Zheng, D., Sun, S., Tian, J., Zhou, M., 2014. Crustal and uppermost mantle velocity structure and its relationship with the formation of ore districts in the middle–lower yangtze river region. Earth and Planetary Science Letters 408, 378–389.

Pavlis, N., Holmes, S., Kenyon, S., Factor, J., 2012. The development and evaluation of the earth gravitational model 2008 (egm2008). Journal of Geophysical Research: Solid Earth 117.

Qashqai, M., Afonso, J., Yang, Y., 2018. Physical state and structure of the crust beneath the western-central united states from multiobservable probabilistic inversion. Tectonics 37, 3117–3147.

Qiang, Z., Wu, Q., Li, Y., 2021. Upper mantle seismic anisotropy beneath the western and central north china craton. Tectonophysics 816, 229025.

Qiu, N., Xu, W., Zuo, Y., Chang, J., 2015. Meso–cenozoic thermal regime in the bohai bay basin, eastern north china craton. International Geology Review 57, 271–289.

Salajegheh, F., Afonso, J., 2023. The upper mantle geoid for lithospheric structure and dynamics. Journal of Geophysical Research: Solid Earth 128, e2023JB026397.

Salajegheh, F., Afonso, J., Minakov, A., Ajourlou, P., Gaina, C., Ortega-Gelabert, O., 2025. The lithosphere-asthenosphere system beneath the north atlantic and surroundings: Results from multi-observable probabilistic inversions. Geochemistry, Geophysics, Geosystems 26, e2024GC011724.

Schott, B., Schmeling, H., 1998. Delamination and detachment of a lithospheric root. Tectonophysics 296, 225–247.

Schutt, D., Lesher, C., 2006. Effects of melt depletion on the density and seismic velocity of garnet and spinel lherzolite. Journal of Geophysical Research: Solid Earth 111.

Shan, B., Afonso, J., Yang, Y., Grose, C., Zheng, Y., Xiong, X., Zhou, L., 2014. The thermochemical structure of the lithosphere and upper mantle beneath south china: Results from multiobservable probabilistic inversion. Journal of Geophysical Research: Solid Earth 119, 8417–8441.

Shen, W., Ritzwoller, M.H., Kang, D., Kim, Y., Lin, F., Ning, J., Wang, W., Zheng, Y., Zhou, L., 2016. A seismic reference model for the crust and uppermost mantle beneath china from surface wave dispersion. Geophysical Journal International 206.

Sun, J., Liu, C.Z., Wu, F.Y., Yang, Y.H., Chu, Z.Y., 2012. Metasomatic origin of clinopyroxene in archean mantle xenoliths from hebi, north china craton: Trace-element and sr-isotope constraints. Chemical Geology 328, 123–136.

Sun, M., Gao, S., Liu, K., Fu, X., 2020. Upper mantle and mantle transition zone thermal and water content anomalies beneath ne asia: Constraints from receiver function imaging of the 410 and 660 km discontinuities. Earth and Planetary Science Letters 532, 116040.

Sun, Y., Dong, S., Wang, X., Liu, M., Zhang, H., Shi, Y., 2022. Three-dimensional thermal structure of east asian continental lithosphere. Journal of Geophysical Research: Solid Earth 127, e2021JB023432.

Tang, Y.J., Zhang, H.F., Ying, J.F., 2006. Asthenosphere–lithospheric mantle interaction in an extensional regime: implication from the geochemistry of cenozoic basalts from taihang mountains, north china craton. Chemical Geology 233, 309–327.

Tao, K., Grand, S., Niu, F., 2018. Seismic structure of the upper mantle beneath eastern asia from full waveform seismic tomography. Geochemistry, Geophysics, Geosystems 19, 2732–2763.

Tarantola, A., 2005. Inverse problem theory and methods for model parameter estimation. SIAM.

Wang, Y., Liu, S., Chen, C., Jiang, G., Wu, J., Guo, L., Wang, Y., Zhang, H., Wang, Z., Jiang, X., Zhu, C., Zuo, Y., Hu, J., Zhang, C., He, L., Hu, S., Pang, Z., Wang, J., 2024. Compilation of terrestrial heat flow data in continental china (5th edition). Chinese Journal of Geophysics 67, 4233–4265. (in chinese).

Xia, B., Thybo, H., Artemieva, I., 2020. Lithosphere mantle density of the north china craton. Journal of Geophysical Research: Solid Earth 125, e2020JB020296.

Xiao, X., Cheng, S., Wu, J., Wang, W., Sun, L., Wang, X., Wen, L., 2021. Shallow seismic structure beneath the continental china revealed by p-wave polarization, rayleigh wave ellipticity and receiver function. Geophysical Journal International 225, 998–1019.

Xu, X., Zhao, L., Wang, K., Yang, J., 2018. Indication from finite-frequency tomography beneath the north china craton: The heterogeneity of craton destruction. Science China Earth Sciences 61, 1238–1260.

Xu, Y., Ma, J., Frey, F.A., Feigenson, M., Liu, J., 2005. Role of lithosphere–asthenosphere interaction in the genesis of quaternary alkali and tholeiitic basalts from datong, western north china craton. Chemical Geology 224, 247–271.

Xu, Y.G., Chung, S.L., Ma, J., Shi, L., 2004. Contrasting cenozoic lithospheric evolution and architecture in the western and eastern sino-korean craton: constraints from geochemistry of basalts and mantle xenoliths. The Journal of Geology 112, 593–605.

Zhang, A., Chu, R., Zhou, P., Yu, C., Yang, Y., 2025a. Extent and mechanisms of the north china craton lithospheric destruction revealed by multi-geophysical inversions. Journal of Geophysical Research: Solid Earth 130, e2025JB031104.

Zhang, R.M., Li, Z.H., Fu, H.Y., Leng, W., Shi, Y.N., Morgan, J., 2025b. 2d versus 3d numerical simulations of mantle plume and lithosphere interaction: Quantitative comparison and scaling analysis. Journal of Geophysical Research: Solid Earth 130, e2025JB031510.

Zhang, Y., Chen, L., Ai, Y., Jiang, M., 2019. Lithospheric structure beneath the central and western north china craton and adjacent regions from s-receiver function imaging. Geophysical Journal International 219, 619–632.

Zhao, G., Sun, M., Wilde, S., Li, S., 2005. Late archean to paleoproterozoic evolution of the north china craton: key issues revisited. Precambrian Research 136, 177–202.

Zheng, J., Griffin, W., O'Reilly, S.Y., Yu, C., Zhang, H., Pearson, N., Zhang, M., 2007. Mechanism and timing of lithospheric modification and replacement beneath the eastern north china craton: Peridotitic xenoliths from the 100 ma fuxin basalts and a regional synthesis. Geochimica et Cosmochimica Acta 71, 5203–5225.

Zhong, S., Wu, J., Si, Z., Zhu, H., Wang, W., 2024. 3d high-resolution s-wave velocity structure of the lithosphere beneath north china craton based on eikonal surface wave tomography. Acta Seismologica Sinica 46, 578–599. (in Chinese).

Zhu, R., Xu, Y., 2019. The subduction of the west pacific plate and the destruction of the north china craton. Science China Earth Sciences 62, 1340–1350.

Zhu, R., Yang, J., Wu, F., 2012. Timing of destruction of the north china craton. Lithos 149, 51–60.

Zhu, T., Ma, X., 2021. Uppermantle shear-wave splitting measurements in mainland china: A review. Earth-Science Reviews 212, 103437.

Supplementary Information for: Imaging Lithosphere–Asthenosphere Interaction Beneath the North China Craton: Implications for Intraplate Volcanism and Anomalous Basin Subsidence

---

Text S1. Construction of Dispersion Curves in Peripheral Regions

The primary tomography model from which we extracted dispersion curves is that of Zhong et al. (2024). However, this study did not provide coverage for certain regions along the margins of the modeled area. To supplement these peripheral regions, we added dispersion curves from two additional studies: Shen et al. (2016) (hereafter S2016) and the recent SinoScope1.0 full-waveform velocity model Ma et al. (2022). Model S2016 is based on a combined ambient-noise and earthquake Rayleigh-wave tomography of mainland China, built from observations at more than 2,000 seismic stations. Its main period range is from 8 to 50 sec, but in parts of South China and Northeast China they extend up to 70 sec. Dispersion curves in the period range 10-140 sec were calculated from model SinoScope1.0 using the forward-modeling code *disp*96 (Herrmann, 2002).

A comparison of these two models is shown in Figure S2. Despite relatively small, localized discrepancies in amplitude, the S2016 and SinoScope1.0 models are highly consistent in their first-order features, particularly in the period range of 20–70 sec. We therefore constructed dispersion curves spanning the 10–140 s period range in the peripheral regions by combining results from the S2016 and SinoScope1.0 models (see Figure S1). Below 35 sec, we only use the dispersion curves from S2016; above 70 sec, we only use those obtained from SinoScope1.0. In the overlapping region (35-70 sec), we use a weighted average (i.e. a smooth, linear taper) that gradually merges the velocities of both models.

We emphasize that the peripheral regions are included primarily for regional completeness and context and they do not influence the main interpretations or conclusions presented in this study.

Text S2. Statistical inference approach to the Inverse Problem

The posterior probability distribution function (PDF) is given by:

$$\mathcal{P}(\boldsymbol{m}) \propto \rho(\boldsymbol{m}) L(\boldsymbol{m}) \tag{S1}$$

where $\rho(\boldsymbol{m})$ denotes the prior PDF, which encodes information about the model parameters independently of the data, and $L(\boldsymbol{m})$ is the likelihood function, which quantifies the probability of observing the data given a model. In the typical case of independent and identically (normally) distributed observations, we can adopt the following form for the likelihood function:

$$L(\boldsymbol{m}) \propto \exp\left[-\frac{1}{2}\sum_{j}\Phi(\boldsymbol{m})_j\right] \tag{S2}$$

where

$$\Phi(\boldsymbol{m})_j = \sum_{i}\left[\frac{\mathbf{d}_i^p - \mathbf{d}_i^o}{\sigma_i}\right]_j^2 \tag{S3}$$

is the misfit function. Here, $\mathbf{d}^p$ and $\mathbf{d}^o$ denote the predicted and observed data, respectively; indices j and i refer to the data type (e.g., elevation, geoid, SHF, dispersion curves, and P velocities) and the individual data points, respectively; and σ_i is the uncertainty associated with each data type at point i.

To obtain estimates of the multidimensional posterior PDF, $\mathcal{P}(\boldsymbol{m})$, we use the Markov Chain Monte Carlo (MCMC) method based on the Delayed Rejection Adaptive Metropolis (DRAM) algorithm (Haario et al., 2006; Shan et al., 2014). Following previous studies (e.g., Afonso et al., 2016; Qashqai et al., 2018; Guo et al., 2016; Shan et al., 2014), we performed 325,000 simulations in each column making up the region of interest (i.e., more than 321×10^6 simulations per inversion). Of these, the first 125,000 iterations constituted a pre-adaptive phase, after which the proposal distribution was updated every 25,000 samples (Haario et al., 2006). Each simulation involves solving the following forward problems: a) computing the thermal structure of the entire lithosphere and sublithospheric upper mantle; b) determining stable mineral assemblages in the mantle via Gibbs free-energy minimization; c) calculating bulk physical properties (e.g., V_p, V_s, and bulk density) of the crust and upper mantle; d) calculating Rayleigh wave dispersion curves; and e) computing geoid height and elevation. Details on the modeling procedures can be found in Afonso et al. (2013a,b, 2016).

Text S3. Yield Envelope and Effective Elastic Thickness

To assess the lithospheric effective elastic thickness (T_e) of our research region, we first calculated the yield strength (or yield envelope) as function of depth for both brittle and ductile deformation mechanisms. These calculations used the density and thermal structure retrieved from our inversion. The brittle field can be described by Byerlee's law (Byerlee, 1978):

$$\sigma_b = \alpha \rho g z (1 - \lambda), \tag{S4}$$

where α is a parameter depending on the type of faulting, ρ is density, g is acceleration of gravity, z is depth (km); λ is the pore fluid factor. In this study, we set typical values of $g = 9.81, \lambda = 0.37$, and $\alpha = 0.75$ (Wang, 2001). The ductile field can be approximated by a power-law dislocation creep Kirby (1983):

$$\sigma_d = \left(\frac{\dot{\varepsilon}}{A_p}\right)^{\frac{1}{n}} \exp\left(\frac{Q}{nRT}\right), \tag{S5}$$

where $\dot{\varepsilon}$ represents the strain rate, A_p is the power strain rate; n is the stress exponent; Q is the activation energy; R is the gas constant; and T is the absolute temperature. Here, we set $\dot{\varepsilon} = 10^{-15} s^{-1}$, $R = 8.31447 J\, mol^{-1} K^{-1}$ (Tesauro et al., 2015). The rheological parameters for each lithospheric layer are shown in Table S1 (e.g., Zang et al., 2005). The yield strength at any given point is defined as the minimum of these two mechanisms:

$$\sigma = \min(\sigma_b, \sigma_d). \tag{S6}$$

From the computed yield envelope, we can estimate the thickness of the mechanically competent part of the lithosphere (Δh_i) by adding all depth intervals where the strength is less than a threshold value (e.g., 10MPa in Ranalli, 1994). Therefore, lithospheric layers are considered coupled or decoupled based on whether the strength decreases below this threshold. For a lithosphere composed of n mechanically competent layers that are decoupled from one another, Te is estimated using the following equation (Burov and Diament, 1995):

$$T_e = \left(\sum_{i=1}^{n} \Delta h_i^3 \right)^{\frac{1}{3}}. \tag{S7}$$

In contrast, if the layers are coupled, Te is simply the total thickness of the mechanically competent layers:

$$T_e = \left(\sum_{i=1}^{n} \Delta h_i \right). \tag{S8}$$

The Te of North China lithosphere is shown in Figure S3, the T_e of BBB region is estimated to be 15–25 km.

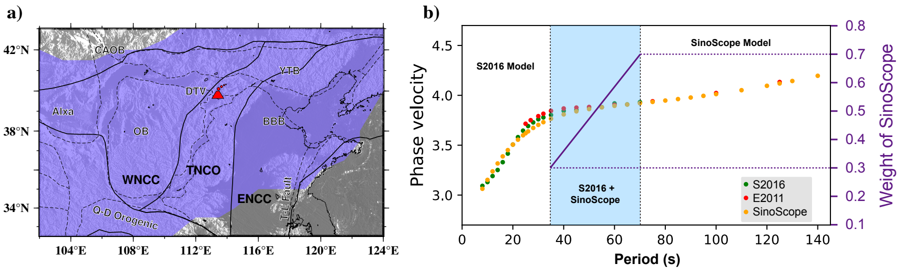

Figure S1: (a) Study area with high-resolution dispersion curves from Zhong et al. (2024) (purple patch). (b) Example of dispersion curves at a randomly selected location in a non-high-resolution region. Three types of dispersion curves are shown as colored points: S2016, E2011 (Göran and Ekström, 2011) and SinoScope1.0. The modified dispersion curve is constructed by merging S2016 and SinoScope1.0, with the weight of the SinoScope1.0 curve (purple line, right axis) varying linearly with period.

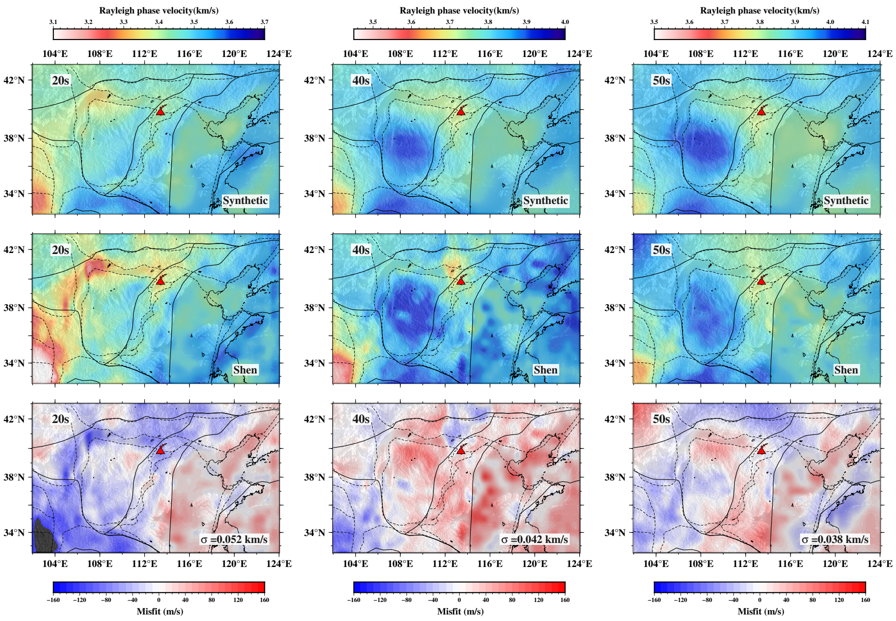

Figure S2: Comparison of phase velocities from models S2016 and SinoScope1.0 at periods of 20, 40 and 50 sec.

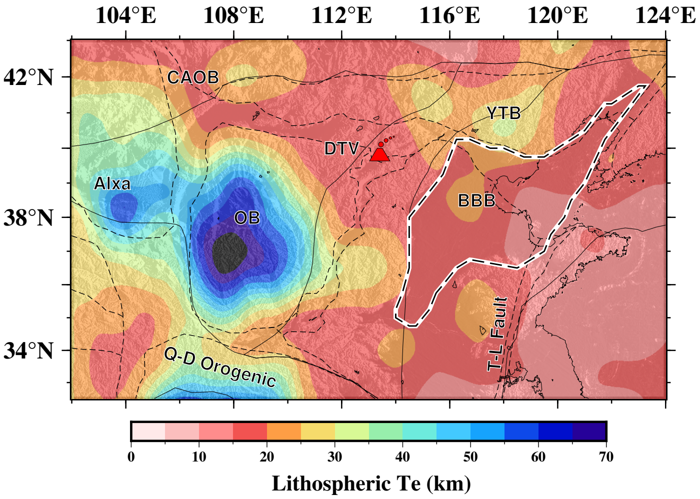

Figure S3: Effective elastic thickness (T_e) of the lithosphere (in km). The area surrounded by the white dash line denote the Bohai Bay Basin (BBB).

Table S1: Rheological parameters of lithospheric layers (Ranalli, 1994, 1997)

Layer	Composition	$A_p(MPa^{-n}s^{-1})$	n	$Q(KJ\,mol^{-1})$
Upper crust	Granitite	1.8×10^{-9}	3.2	123
Middle/Lower crust	Felsic granulite	0.8×10^{-4}	3.1	243
Upper mantle	Wet peridotite	2.5×10^{3}	4.5	532

Table S2: Constant crustal parameters

	Thermal conductivity ($Wm^{-1}\,°C^{-1}$)	Thermal expansion ($°C^{-1}$)	Thermal compressibility (Pa^{-1})
Three-crustal layers			
Sediment	2.5	2.7×10^{-5}	5.0×10^{-11}
Crstalline 1	2.4	2.6×10^{-5}	1.4×10^{-11}
Crstalline 2	2.2	2.3×10^{-5}	1.1×10^{-11}
Four-crustal layers			
Sediment	2.4	2.7×10^{-5}	5.0×10^{-11}
Crstalline 1	2.5	2.4×10^{-5}	1.7×10^{-11}
Crstalline 2	2.2	2.3×10^{-5}	1.4×10^{-11}
Crstalline 3	2.0	2.1×10^{-5}	1.2×10^{-11}

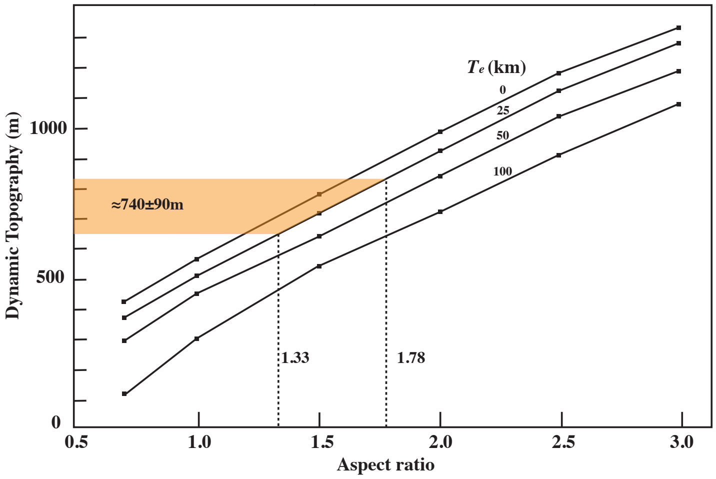

Figure S4: The dynamic topography at subsidence center which depending on aspect ratio of the convection and effective elastic thickness T_e.(Modified from Marquart and Schmeling, 1989). In our study, the aspect ratio of convection cell is approximated between 1.33 to 1.78, and we conservatively use $T_e = 25$ km as a representative value in BBB, so that the dynamic topography driven by the mantle convection approximate 740±90 m.

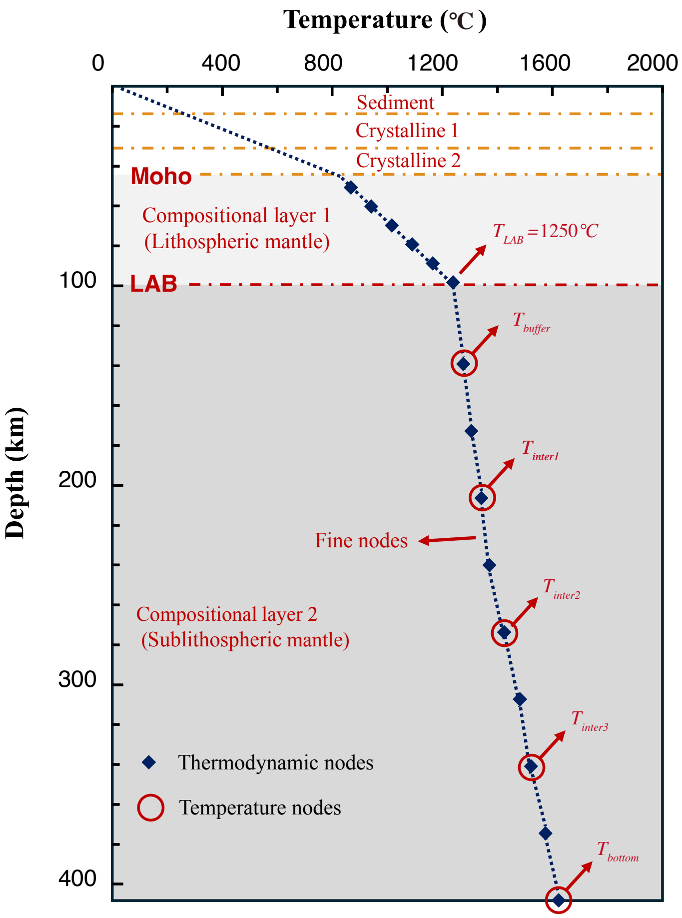

Figure S5: Model parameterization (modified from Afonso et al., 2016). This model shows a 3-layer crust structure with 5 temperature nodes in the sub-lithospheric mantle (characteristic of a thin LAB). A finite-difference mesh with 2 km resolution (blue dots) discretizes the entire column and is used to solve the forward problems related to the steady-state heat transfer equation, gravity potential, and isostatic balance for temperature, geoid height, and elevation, respectively. In the mantle, 15 thermodynamic nodes (blue diamonds) are introduced to calculate thermophysical properties (e.g., V_p, V_s, ρ). These properties are derived by minimizing Gibbs free-energy using components of the Perple_X software (Connolly, 2009) and the thermodynamic database and formalism of Stixrude and Lithgow-Bertelloni (2011).

a. Ordos Block—Lon 109.5° Lat 37°

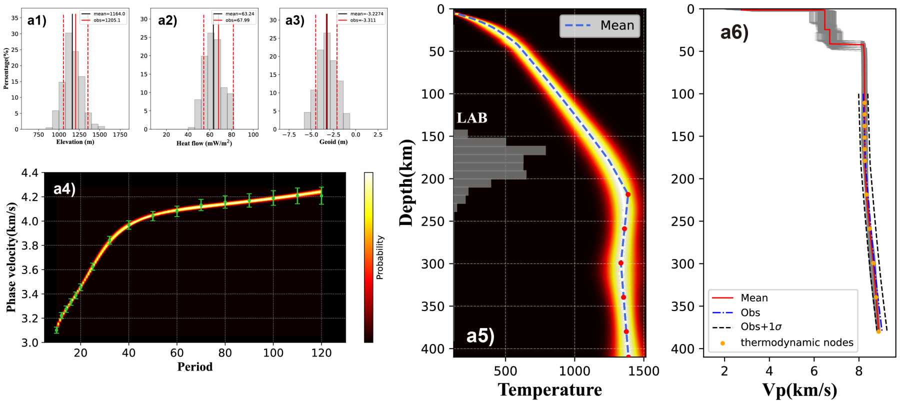

b. Datong Volcanic field—Lon 112° Lat 39°

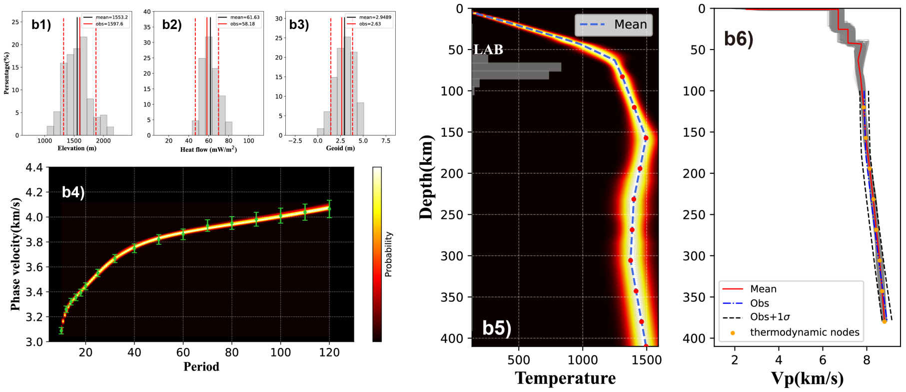

c. Bohai Bay Basin—Lon 118.5° Lat 36.5°

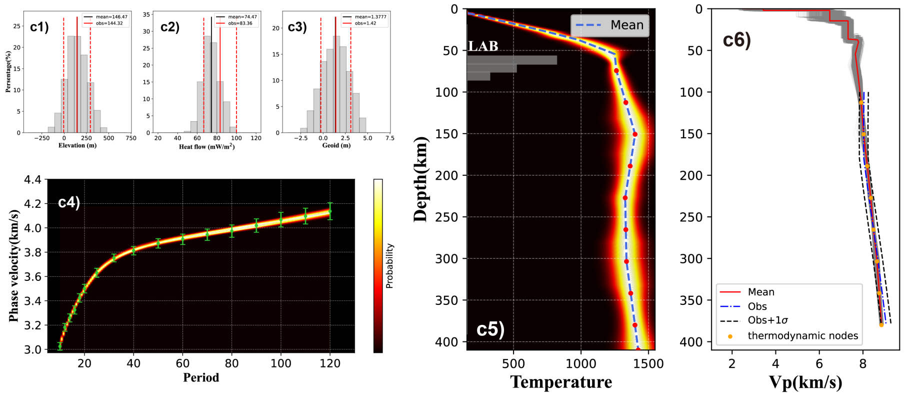

Figure S6: Posterior probability density functions (PDFs) of key parameters at three representative tectonic locations: (a) Ordos Block, (b) Datong Volcanic Field, and (c) Bohai Bay Basin. Panels (a1-c3) show posterior histograms of surface elevation, surface heat flow, and geoid height. Red solid lines denote observations, red dashed lines their uncertainties, and black solid lines the mean of accepted models. Panels (a4–c4) display observed Rayleigh-wave dispersion curves (green error bars) compared with predictions from accepted models. Panels (a5–c5) present temperature–depth profiles, where blue dashed lines indicate posterior means, red dots mark thermodynamic nodes in the sublithospheric mantle, and grey histograms along the vertical axis represent the posterior distributions of LAB depth. Panels (a6–c6) show posterior PDFs of P-wave velocity (grey) with the mean (red solid line), observed values from the SinoScope model (Ma et al., 2022) (blue dashed line), and associated uncertainties (black dashed line, ±2% Vp). Only mantle thermodynamic nodes deeper than 100 km (yellow dots) are used in the fitting.

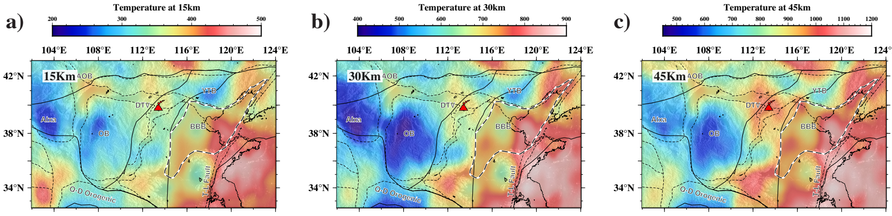

Figure S7: Predicted shallow thermal structure at 15, 30 and 45 km depth from our model.

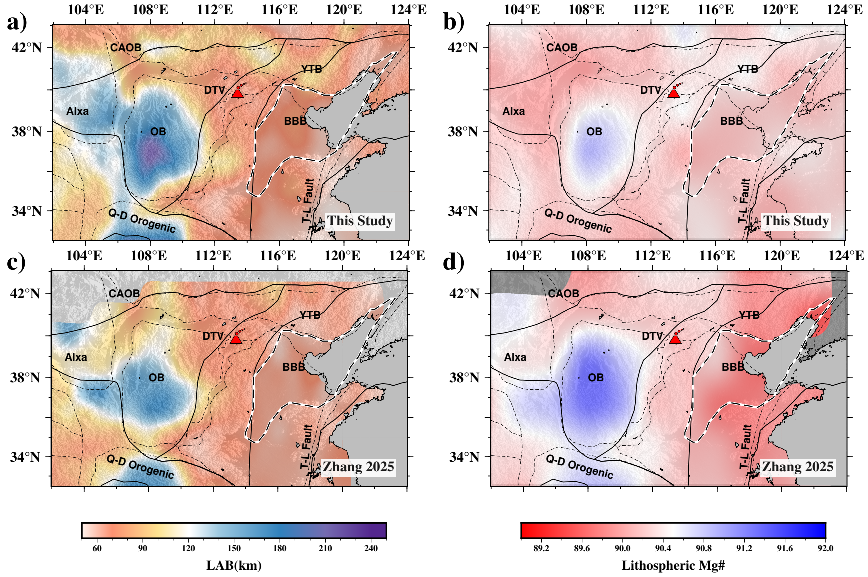

Figure S8: Comparison of thermal lithospheric thickness and Mg# from this study and from that of Zhang et al. (2025). (a-b) show LAB depth and Mg# from this study; (c-d) from Zhang et al. (2025).

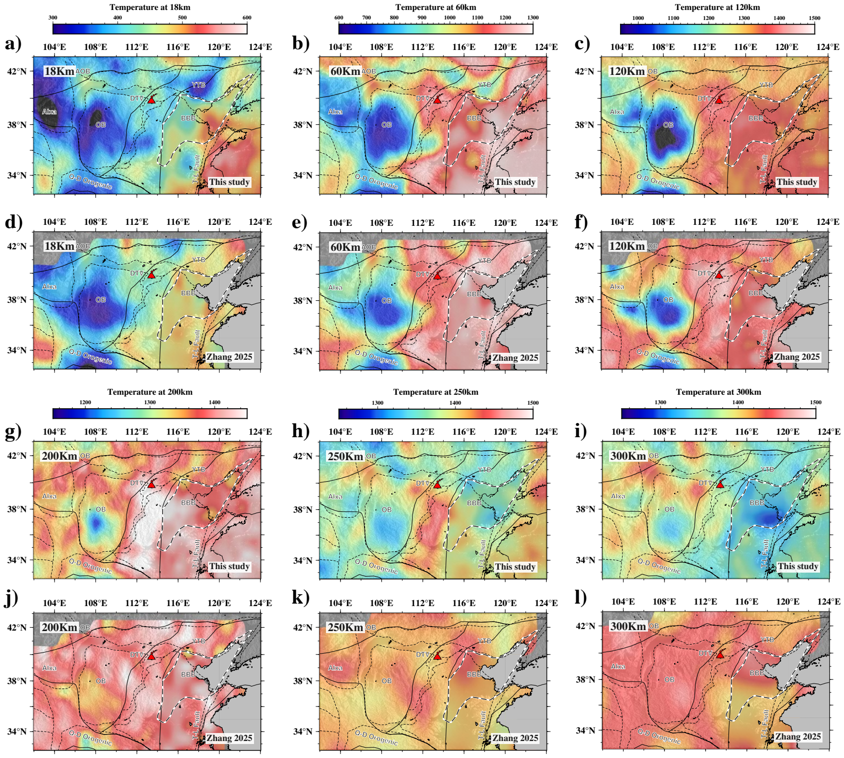

Figure S9: Comparison of thermal structures as predicted by this study and that of Zhang et al. (2025). (a-c) and (g-i) are results from this study; (d-f) and (j-l) from Zhang et al. (2025).

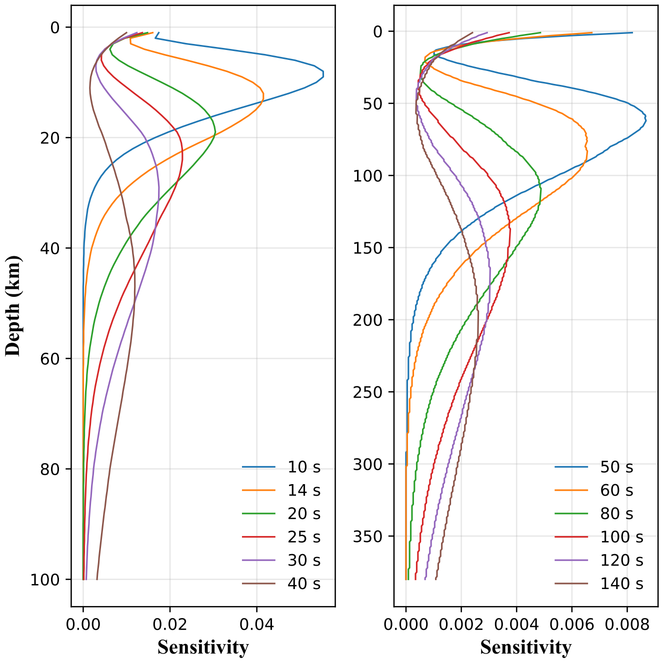

Figure S10: Sensitivity kernel curves of Rayleigh wave phase velocity to shear wave velocity at different periods (a)10–40s; (b)50–140s

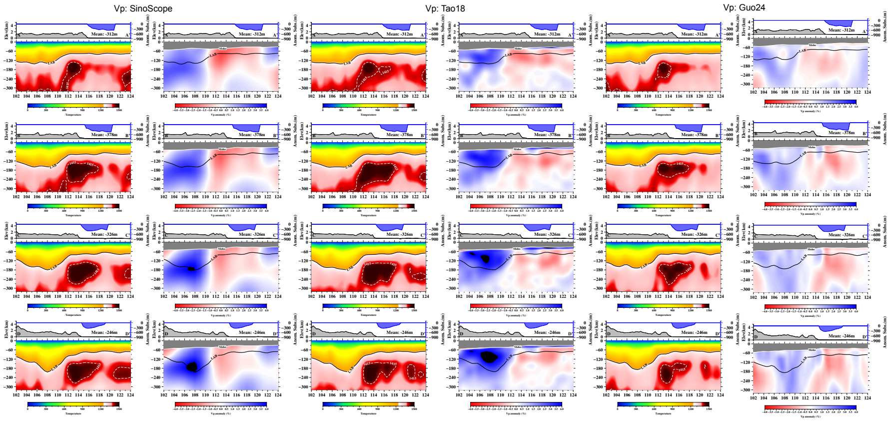

Figure S11: Vertical sections of inverted thermal structure (columns 1, 3, and 5) and corresponding V_p velocity anomalies (columns 2, 4, and 6) along the same profiles as shown in Figure 8. The three pairs of columns are based on different V_p models used in the joint inversion: SinoScope1.0 (columns 1-2, Ma et al., 2022), Tao18 (columns 3–4 Tao et al., 2018), and Guo24 (columns 5–6 Guo et al., 2024).

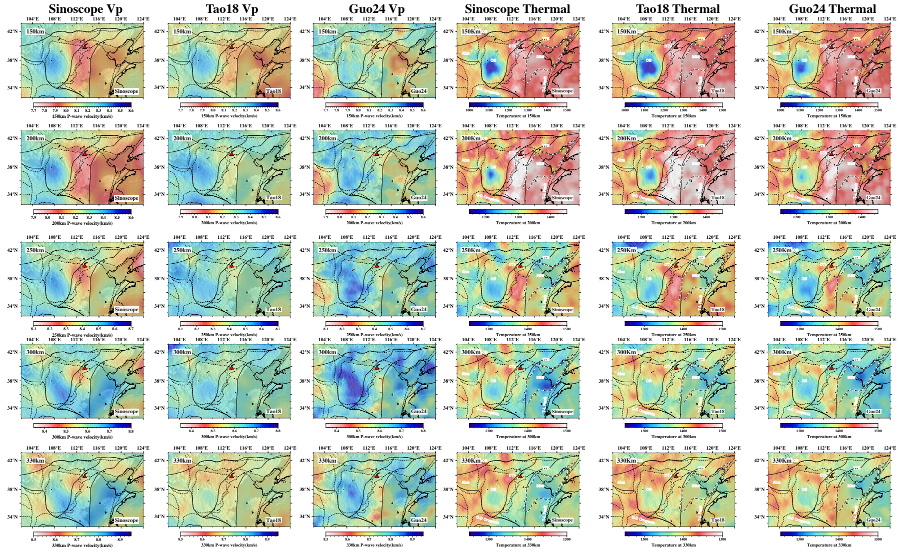

Figure S12: Horizontal slices of V_p velocity (columns 1–3) at different depths based on three tomographic models (same as Figure.S11), and the corresponding inverted temperature structures (columns 4–6) derived from joint inversion constrained by each respective V_p model.

Vp model: Tao18

a. Ordos Block—Lon 109.5° Lat 37°

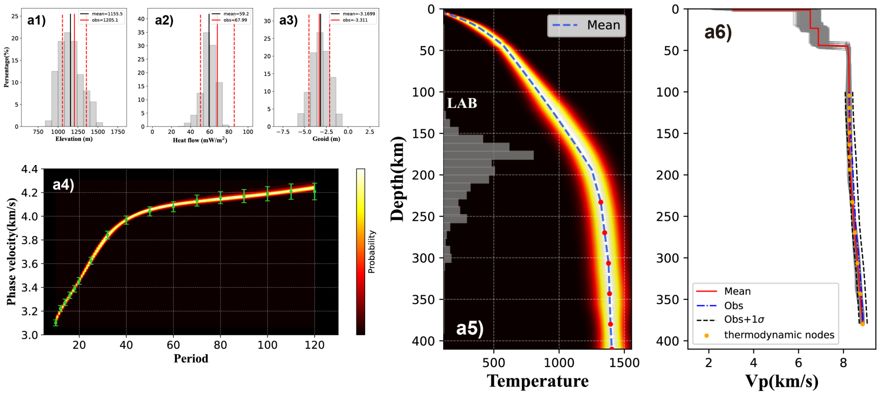

b. Datong Volcanic field—Lon 112° Lat 39°

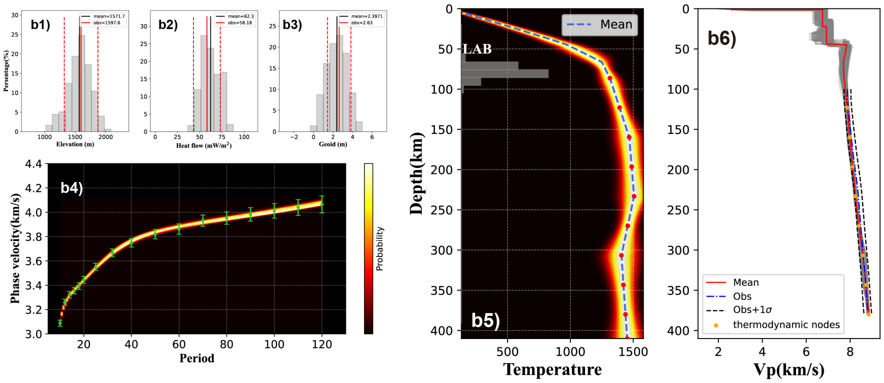

c. Bohai Bay Basin—Lon 118.5° Lat 36.5°

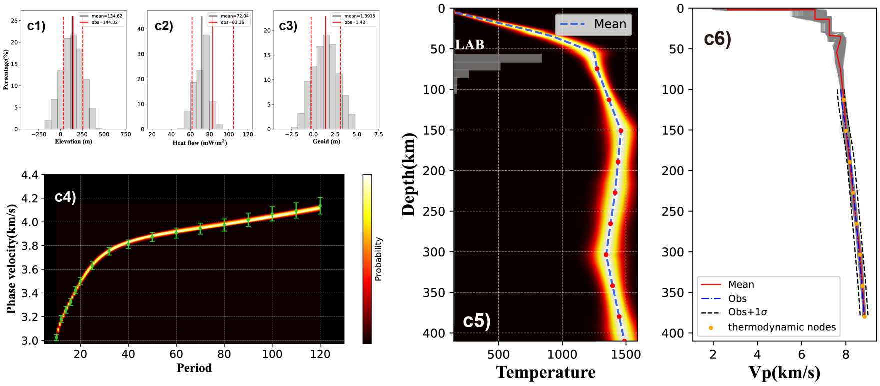

Figure S13: The same as FigureS6 but with Tao18 V_p model.

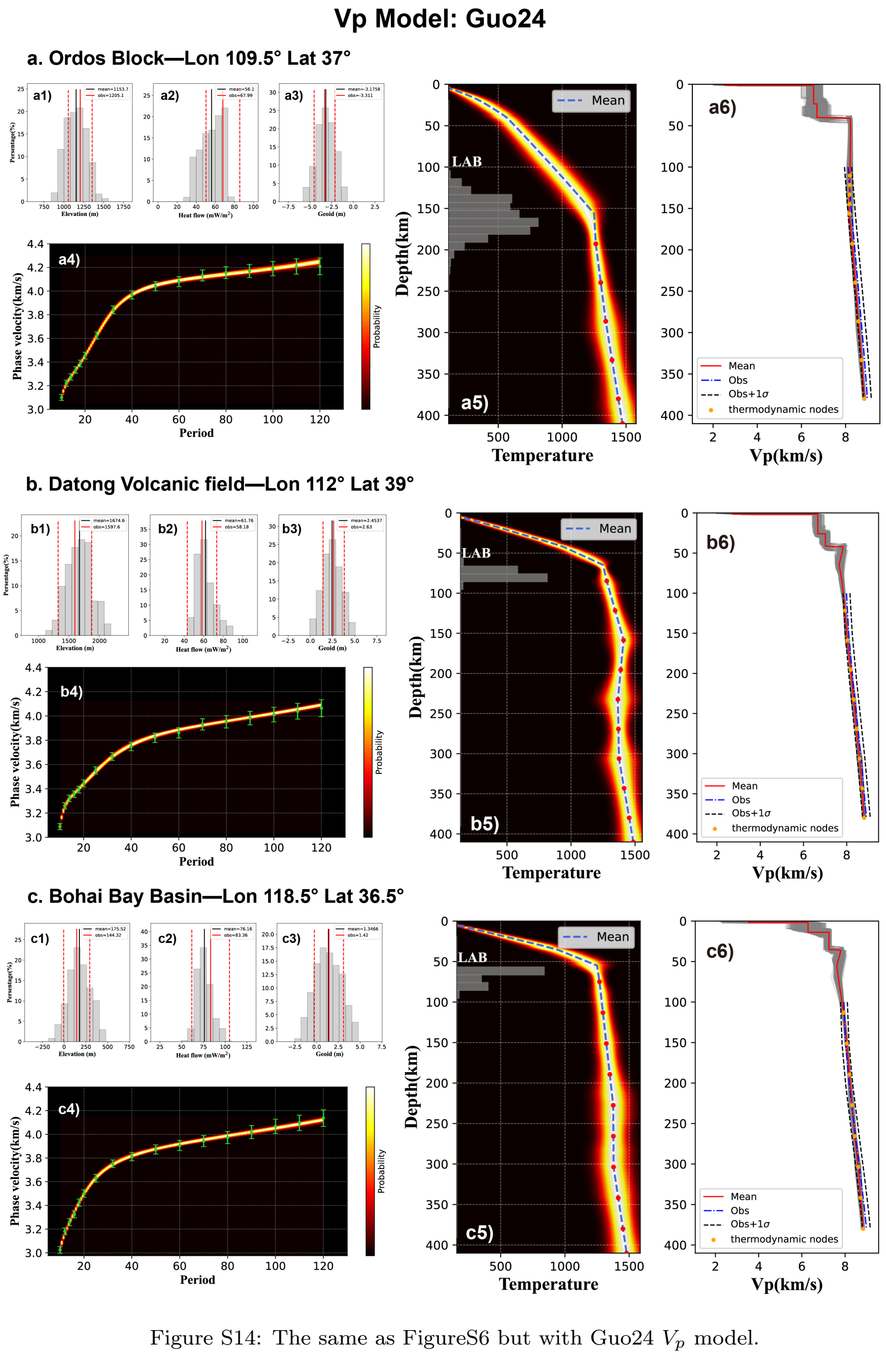

Figure S14: The same as FigureS6 but with Guo24 V_p model.

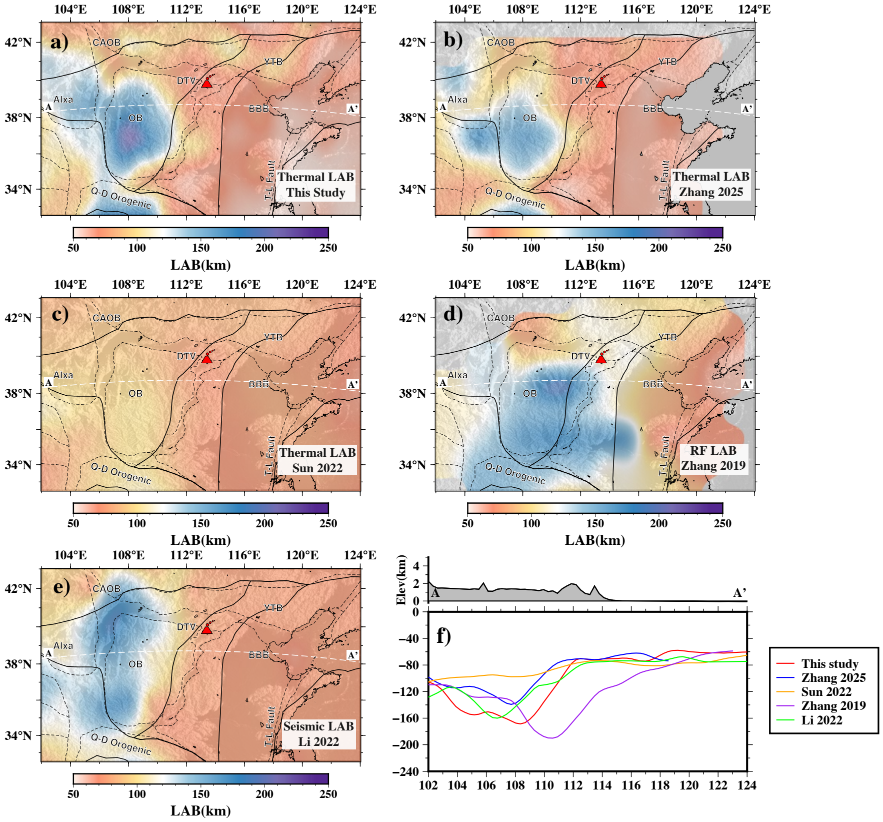

Figure S15: Comparison of LAB depths derived from different methods and definitions. (a) Thermally defined LAB from this study; (b) thermally defined LAB from Zhang et al. (2025), who applied a similar inversion framework but used different datasets; (c) thermal LAB extracted from Sun et al. (2022), defined by the 1250 °C isotherm, where mantle thermal structure was inferred solely from an S-wave tomographic model (Huang et al., 2003); (d) LAB inferred from receiver function analysis (Zhang et al., 2019); (e) seismic LAB defined as the depth of the maximum negative velocity gradient in the tomographic model of Li et al. (2022). (f) LAB depth variations along profile A–A′ for all models.

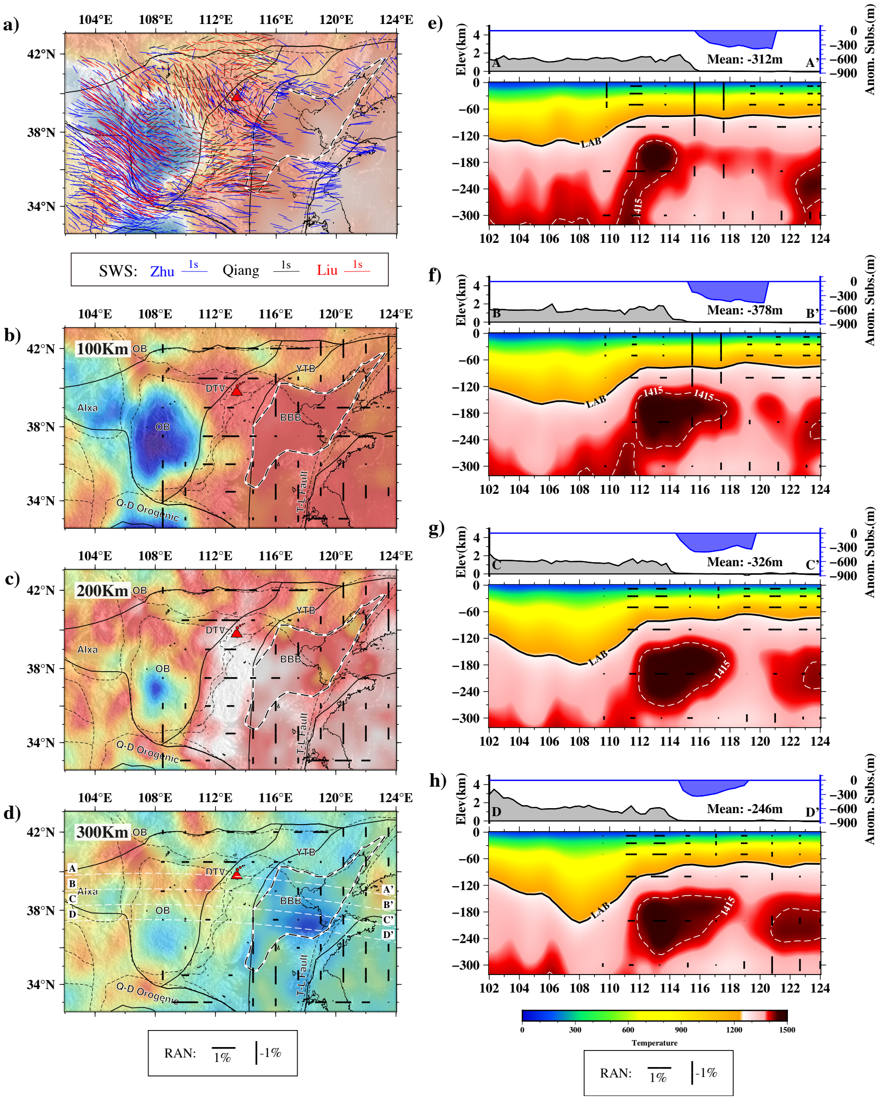

Figure S16: Regional shear-wave splitting (SWS), radial anisotropy (RAN), and their relationship with the inverted thermal structure. (a) Compilation of fast polarization directions from recent SWS studies (Zhu and Ma, 2021; Qiang et al., 2021; Liu et al., 2021). (b–d) Horizontal slices of the inverted temperature structure at depths of 100 km, 200 km, and 300 km, respectively, with radial anisotropy (from Liang et al., 2022) superimposed. (e–h) Vertical sections of the temperature model along profiles A–A′ to D–D′, with RAN (Liang et al., 2022) variations overlain. The locations of these profiles are shown in (d) and are identical to those in Figure 8.

Table S3: Model parameters and their prior ranges

Model Parameters	Range
Crust	
RHP ($\mu W/m^3$)	0.1-2.6
Density (Sediment, kg/m^3)	2100-2750
Density (crystalline 1, kg/m^3)	2400-2950
Density (crystalline 2 or 3, kg/m^3)	2500-3200
Thickness perturbation (Sediment, km)	-2.0-2.0
Thickness perturbation (crystalline 1, km)	-5.0-5.0
Thickness perturbation (crystalline 2 or 3, km)	-7.0-7.0
V_P/V_S (Sediment)	1.65-2.25
V_P/V_S (crystalline 1)	1.65-1.90
V_P/V_S (crystalline 2 or 3)	1.65-2.15
Mantle	
LAB depth (km)	45-300
Al_2O_3 in the lithosphere (wt. %)	0.5-5.5
FeO in the lithosphere (wt. %)	6-9.2
MgO in the lithosphere (wt. %)	34-51
CaO in the lithosphere (wt. %)	0.1-5.5
Al_2O_3 in the sublithospheric mantle (wt. %)	1.5-5.5
FeO in the sublithospheric mantle (wt. %)	7-9.2
MgO in the sublithospheric mantle (wt. %)	34-46
CaO in the sublithospheric mantle (wt. %)	1.5-5.5
T_{buffer} ($^\circ C$)	1200-1500
T_{inter1} ($^\circ C$)	1230-1530
T_{inter2} ($^\circ C$)	1250-1550
T_{inter3} ($^\circ C$)	1300-1600
T_{bottom} ($^\circ C$)	1350-1680

[1] This RHP value is only used in the sedimentary and first crystalline layers, for the deeper crystalline layers, RHP/10 are assumed.

[2] Si_2O is computed as $100 - (Al_2O_3 + FeO + MgO + CaO)$.

[3] The research region primarily follows a three-layer crust model, which does not include the “crystalline 3” layer.

[4] For definitions of "temperature nodes", see Fig.S5. In the region with a very thick LAB, there are only 3 "temperature nodes" assigned, excluding T_{inter1} and T_{inter2}.

References

Afonso, J., Fullea, J., Griffin, W., Yang, Y., Jones, A., Connolly, J., O'Reilly, S., 2013a. 3-d multiobservable probabilistic inversion for the compositional and thermal structure of the lithosphere and upper mantle. i: a priori petrological information and geophysical observables. Journal of Geophysical Research: Solid Earth 118, 2586–2617.

Afonso, J., Fullea, J., Yang, Y., Connolly, J., Jones, A., 2013b. 3-d multiobservable probabilistic inversion for the compositional and thermal structure of the lithosphere and upper mantle. ii: General methodology and resolution analysis. Journal of Geophysical Research: Solid Earth 118, 1650–1676.

Afonso, J., Rawlinson, N., Yang, Y., Schutt, D., Jones, A., Fullea, J., Griffin, W., 2016. 3-d multiobservable probabilistic inversion for the compositional and thermal structure of the lithosphere and upper mantle:iii. thermochemical tomography in the western-central u.s. Journal of Geophysical Research: Solid Earth 121, 7337–7370.

Burov, E.B., Diament, M., 1995. The effective elastic thickness (te) of continental lithosphere: What does it really mean? Journal of Geophysical Research: Solid Earth 100, 3905–3927.

Byerlee, J., 1978. Friction of rocks. Rock friction and earthquake prediction , 615–626.

Connolly, J., 2009. The geodynamic equation of state: what and how. Geochemistry, geophysics, geosystems 10.

Guo, H., Zhao, D., Ding, Z., 2024. Anisotropic tomography and mantle dynamics of the north china craton. Geophysical Journal International 236, 1455–1470.

Guo, Z., Afonso, J., Qashqai, M., Yang, Y., Chen, Y., 2016. Thermochemical structure of the north china craton from multi-observable probabilistic inversion: Extent and causes of cratonic lithosphere modification. Gondwana Research 37, 252–265.

Göran, Ekström, 2011. A global model of love and rayleigh surface wave dispersion and anisotropy, 25–250 s. Geophysical Journal International 187.

Haario, H., Laine, M., Mira, A., Saksman, E., 2006. Dram: efficient adaptive mcmc. Statistics and computing 16, 339–354.

Herrmann, R., 2002. Computer program in seismology, version 3.3. WWW Document. URL: `https://doi.org/10.1007/978-3-322-80338-2`.

Huang, Z., Su, W., Peng, Y., Zheng, Y., Li, H., 2003. Rayleigh wave tomography of china and adjacent regions. Journal of Geophysical Research: Solid Earth 108.

Kirby, S.H., 1983. Rheology of the lithosphere. Reviews of Geophysics 21, 1458–1487.

Li, M., Song, X., Li, J., Bao, X., 2022. Crust and upper mantle structure of east asia from ambient noise and earthquake surface wave tomography. Earthquake Science 35, 71–92.

Liang, X., Zhao, D., Xu, Y., Hua, Y., 2022. Anisotropic tomography and dynamics of the big mantle wedge. Geophysical Research Letters 49, e2021GL097550.

Liu, J., Wu, J., Wang, W., Cai, Y., Fang, L., 2021. Seismic anisotropy and implications for lithospheric deformation beneath the ordos block and surrounding regions. Geophysical Journal International 226, 1885–1896.

Ma, J., Bunge, H., Thrastarson, S., Fichtner, A., Herwaarden, D.V., Tian, Y., Chang, S., Liu, T., 2022. Seismic full-waveform inversion of the crust-mantle structure beneath china and adjacent regions. Journal of Geophysical Research: Solid Earth 127.

Marquart, G., Schmeling, H., 1989. Topography and geoid undulations caused by small-scale convection beneath continental lithosphere of variable elastic thickness. Geophysical Journal International 97, 511–527.

Qashqai, M., Afonso, J., Yang, Y., 2018. Physical state and structure of the crust beneath the western-central united states from multiobservable probabilistic inversion. Tectonics 37, 3117–3147.

Qiang, Z., Wu, Q., Li, Y., 2021. Upper mantle seismic anisotropy beneath the western and central north china craton. Tectonophysics 816, 229025.

Ranalli, G., 1994. Nonlinear flexure and equivalent mechanical thickness of the lithosphere. Tectonophysics 240, 107–114.

Ranalli, G., 1997. Rheology and deep tectonics. Rheology and deep tectonics 40.

Shan, B., Afonso, J., Yang, Y., Grose, C., Zheng, Y., Xiong, X., Zhou, L., 2014. The thermochemical structure of the lithosphere and upper mantle beneath south china: Results from multiobservable probabilistic inversion. Journal of Geophysical Research: Solid Earth 119, 8417–8441.

Shen, W., Ritzwoller, M.H., Kang, D., Kim, Y., Lin, F., Ning, J., Wang, W., Zheng, Y., Zhou, L., 2016. A seismic reference model for the crust and uppermost mantle beneath china from surface wave dispersion. Geophysical Journal International 206.

Stixrude, L., Lithgow-Bertelloni, C., 2011. Thermodynamics of mantle minerals-ii. phase equilibria. Geophysical Journal International 184, 1180–1213.

Sun, Y., Dong, S., Wang, X., Liu, M., Zhang, H., Shi, Y., 2022. Three-dimensional thermal structure of east asian continental lithosphere. Journal of Geophysical Research: Solid Earth 127, e2021JB023432.

Tao, K., Grand, S., Niu, F., 2018. Seismic structure of the upper mantle beneath eastern asia from full waveform seismic tomography. Geochemistry, Geophysics, Geosystems 19, 2732–2763.

Tesauro, M., Kaban, M.K., Mooney, W.D., 2015. Variations of the lithospheric strength and elastic thickness in north america. Geochemistry, Geophysics, Geosystems 16, 2197–2220.

Wang, Y., 2001. Heat flow pattern and lateral variations of lithosphere strength in china mainland: constraints on active deformation. Physics of the Earth and Planetary Interiors 126, 121–146.

Zang, S., Wei, R., Liu, Y., 2005. Three-dimensional rheological structure of the lithosphere in the ordos block and its adjacent area. Geophysical Journal International 163, 339–356.

Zhang, A., Chu, R., Zhou, P., Yu, C., Yang, Y., 2025. Extent and mechanisms of the north china craton lithospheric destruction revealed by multi-geophysical inversions. Journal of Geophysical Research: Solid Earth 130, e2025JB031104.

Zhang, Y., Chen, L., Ai, Y., Jiang, M., 2019. Lithospheric structure beneath the central and western north china craton and adjacent regions from s-receiver function imaging. Geophysical Journal International 219, 619–632.

Zhong, S., Wu, J., Si, Z., Zhu, H., Wang, W., 2024. 3d high-resolution s-wave velocity structure of the lithosphere beneath north china craton based on eikonal surface wave tomography. Acta Seismologica Sinica 46, 578–599. (in Chinese).

Zhu, T., Ma, X., 2021. Uppermantle shear-wave splitting measurements in mainland china: A review. Earth-Science Reviews 212, 103437.